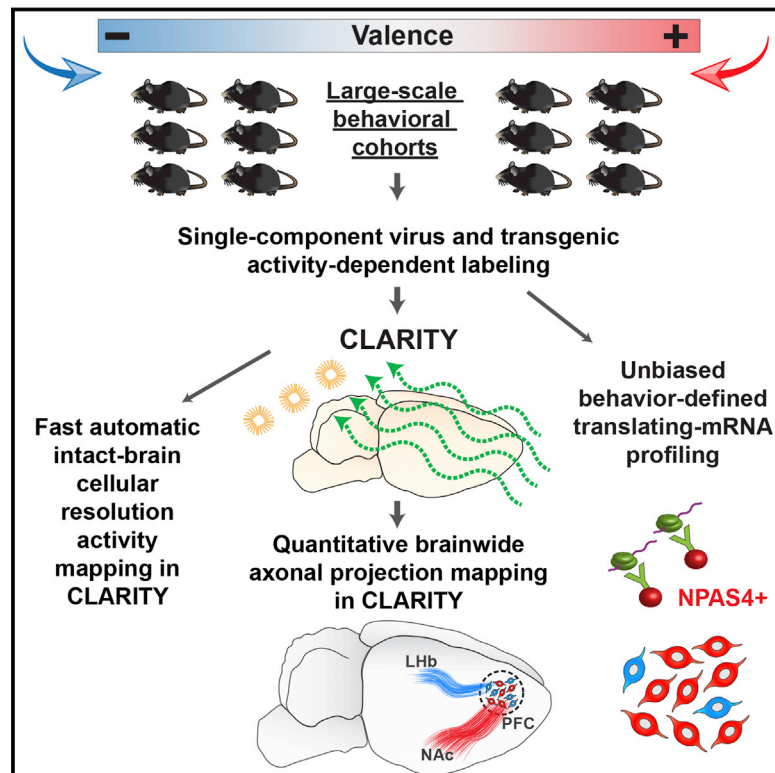# Cell

# Wiring and Molecular Features of Prefrontal Ensembles Representing Distinct Experiences

## Graphical Abstract

## Authors

Li Ye, William E. Allen, Kimberly R. Thompson, ..., Liqun Luo, Jennifer A. McNab, Karl Deisseroth

## Correspondence

deissero@stanford.edu

## In Brief

A quantitative analysis of the wiring and molecular properties of neurons in the prefrontal cortex that are associated with distinct behavioral experiences illuminates the logic of information processing in the brain.

## Highlights

- Cohort-scale CLARITY is enabled for whole-brain activity/projection measurements

- mPFC cells active during distinct-valence experiences exhibit distinct projections

- Positive-valence experience preferentially recruits an NPAS4+ population in mPFC

- Recruiting diverse experience-defined mPFC ensembles drives distinct behaviors

# CellPress

# Article

**Cell**

# Wiring and Molecular Features of Prefrontal Ensembles Representing Distinct Experiences

Li Ye,[1,2,8,10] William E. Allen,[1,3,5,10] Kimberly R. Thompson,[1,10] Qiyuan Tian,[6] Brian Hsueh,[1,2,3] Charu Ramakrishnan,[1,2] Ai-Chi Wang,[1,2] Joshua H. Jennings,[1,2] Avishek Adhikari,[1,2] Casey H. Halpern,[7] Ilana B. Witten,[1] Alison L. Barth,[9] Liqun Luo,[5,8] Jennifer A. McNab,[6] and Karl Deisseroth[1,2,4,8,*]
[1]Department of Bioengineering
[2]CNC Program
[3]Neurosciences Program
[4]Department of Psychiatry
[5]Department of Biology
[6]Department of Radiology
[7]Department of Neurosurgery
[8]Howard Hughes Medical Institute
Stanford University, Stanford, CA 94305, USA
[9]Biological Sciences, Carnegie Mellon University, Pittsburgh, PA 15213, USA
[10]Co-first author
*Correspondence: deissero@stanford.edu
http://dx.doi.org/10.1016/j.cell.2016.05.010

## SUMMARY

A major challenge in understanding the cellular diversity of the brain has been linking activity during behavior with standard cellular typology. For example, it has not been possible to determine whether principal neurons in prefrontal cortex active during distinct experiences represent separable cell types, and it is not known whether these differentially active cells exert distinct causal influences on behavior. Here, we develop quantitative hydrogel-based technologies to connect activity in cells reporting on behavioral experience with measures for both brain-wide wiring and molecular phenotype. We find that positive and negative-valence experiences in prefrontal cortex are represented by cell populations that differ in their causal impact on behavior, long-range wiring, and gene expression profiles, with the major discriminant being expression of the adaptation-linked gene NPAS4. These findings illuminate cellular logic of prefrontal cortex information processing and natural adaptive behavior and may point the way to cell-type-specific understanding and treatment of disease-associated states.

## INTRODUCTION

The many regions and layers of the mammalian prefrontal cortex are known to contain cells with a rich diversity of activity patterns. Indeed, otherwise-indistinguishable populations of principal cells exhibiting profoundly distinct changes in activity in response to stimulus have been characterized by electrophysiological recording and cellular-resolution fluorescence $Ca^{2+}$ imaging (Hayden et al., 2008; Insel and Barnes, 2015; Ito et al.,

2003; Matsumoto et al., 2007; Pinto and Dan, 2015; Warden et al., 2012). At the same time, datastreams of anatomical and molecular information on prefrontal cell typology have emerged from a variety of methods, also pointing toward a rich diversity of principal neurons despite the traditional view that these cells were more homogenous than the highly diverse and readily separable interneurons (Hof et al., 1996; Lee et al., 2014; Soloway et al., 2002). These findings have highlighted the morphological, wiring, and electrophysiological diversity of principal neurons even within individual layers and subregions.

However, the mapping and correspondences (if any) among these different domains of diversity (activity during behavior, long-range wiring, and molecular phenotype) have remained largely unclear within prefrontal cortex. Addressing this issue would have fundamental implications for elucidating the cellular logic of prefrontal cortex function; moreover, differences in wiring, role in behavior, and molecular signatures among differentially responsive cells could provide long-elusive insight into the mechanisms of action of current neuromodulation therapies and even lay the foundation for developing new kinds of cell-targeted disease treatment. But the unique and non-stereotyped nature of each mammalian nervous system has prevented experimental resolution of this fundamental question, since cellular-resolution activity in a brain during behavior would have to be directly linked to quantitative local and global wiring, as well as to molecular analysis of the very same cells in the same mammalian brain, which has not yet been possible. Here, we address this question by developing approaches to quantify long-range anatomy, molecular signatures, and the causal impact of prefrontal cortical cells, defined by activity during distinct experiences.

## RESULTS

### Behavioral Cohort-Scale Whole-Brain Activity Mapping
We began with development and integration of enhanced Arc-TRAP and CLARITY technologies. The ArcTRAP transgenic

**Cell**
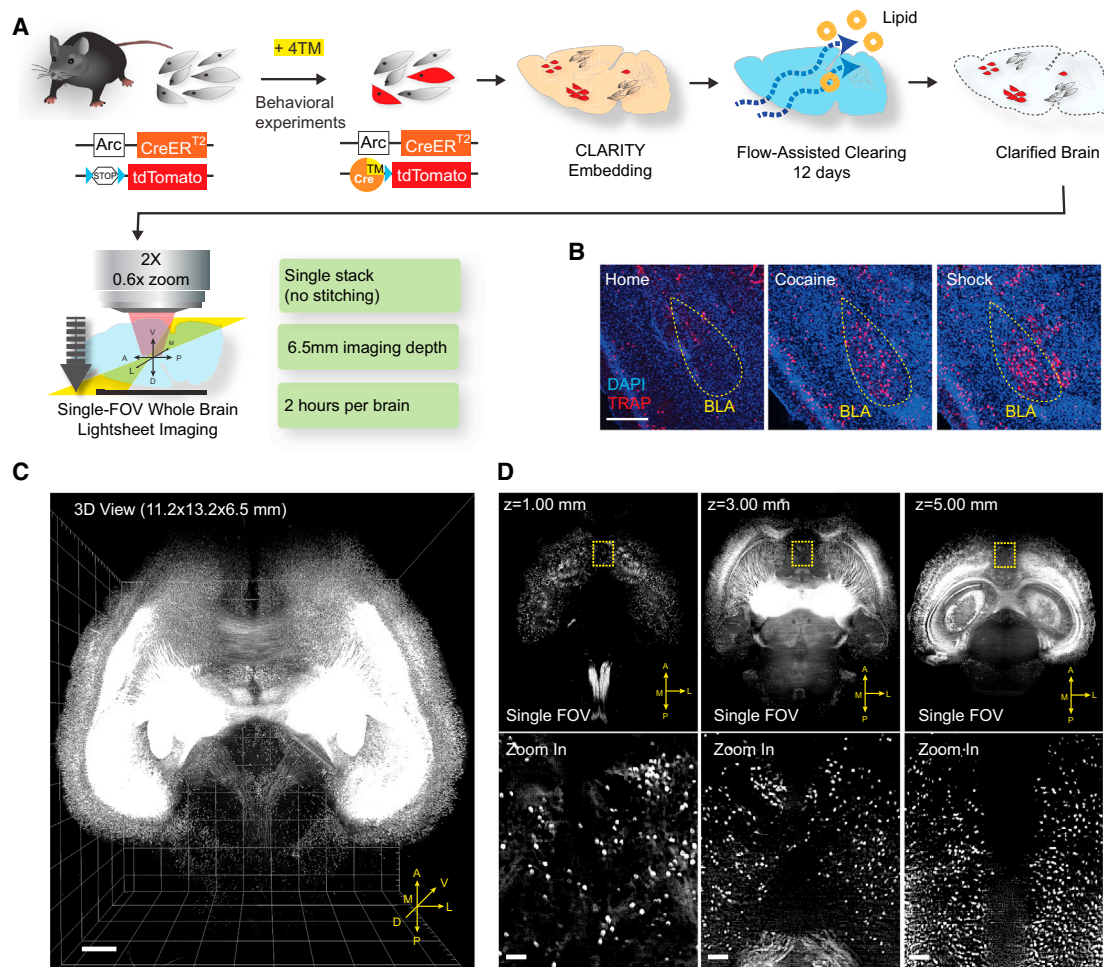


**Figure 1. Behavioral Cohort-Scale Brain-wide Activity Mapping**

(A) Schematic of ArcTRAP labeling and the enhanced cohort-scale CLARITY pipeline for rapid whole-brain clearing and imaging. CreER expression is driven by the activity-dependent *Arc* promoter to mediate 4TM-dependent recombination that permanently labels the active neurons with tdTomato.

(B) Representative confocal images from 40-μm sections showing TRAP labeling in BLA (yellow circle). Scale bar, 400 μm.

(C) 3D rendering of a CLARITY-processed whole-mouse brain (ArcTRAP) imaged by light-sheet microscopy. Scale bar, 500 μm.

(D) Top: single field of view (FOV) images at the indicated imaging depths. Bottom: zoomed-in images from the yellow-boxed regions in the top row showing cellular resolution. Scale bar, 100 μm.

See also Figure S1.

mouse line was previously shown to translate temporally de-limited neuronal activity into fluorescence via CreER/tamoxifen-mediated recombination (Figure 1A) (Guenthner et al., 2013). While the ArcTRAP line had been reported to have high background recombination, we developed an aqueous formulation of the fast-acting tamoxifen (4-hydroxytamoxifen, 4TM) enabling dosage reduction by an order of magnitude; this approach to ArcTRAP was found to eliminate the background recombination (Figures 1B and S1B). ArcTRAP mice can then be exposed to a rewarding or aversive experience (e.g., cocaine dosing at 15 mg/kg or a series of 0.5 mA/2 s foot shocks, respectively) with resulting robust and faithful labeling of neurons (Figure S1A); for example, histology confirmed that both experience types (with comparable but opposite conditioning value; Figures S1C and S1D) recruited

neurons in basolateral amygdala (BLA; which is known to be involved in both reward and aversion processing) (Hsiang et al., 2014) (Figure 1B).

This approach brings untapped potential for obtaining deeper perspective on the cells activated, including insight into brain-wide patterns and molecular properties of cells recruited. Traditional thin-section histology would be prohibitively labor-intensive for whole-brain analysis in large behavioral-scale cohorts and also subject to sampling loss and bias, but the recent emergence of tissue transparency techniques, such as CLARITY, has, in principle, enabled lossless high-resolution brain-wide imaging compatible with molecular analysis (Chung et al., 2013; Tomer et al., 2014), if not yet in large cohorts of subjects. We therefore developed an enhanced CLARITY process suitable for this challenge of large-cohort analysis linked to behavioral experience;
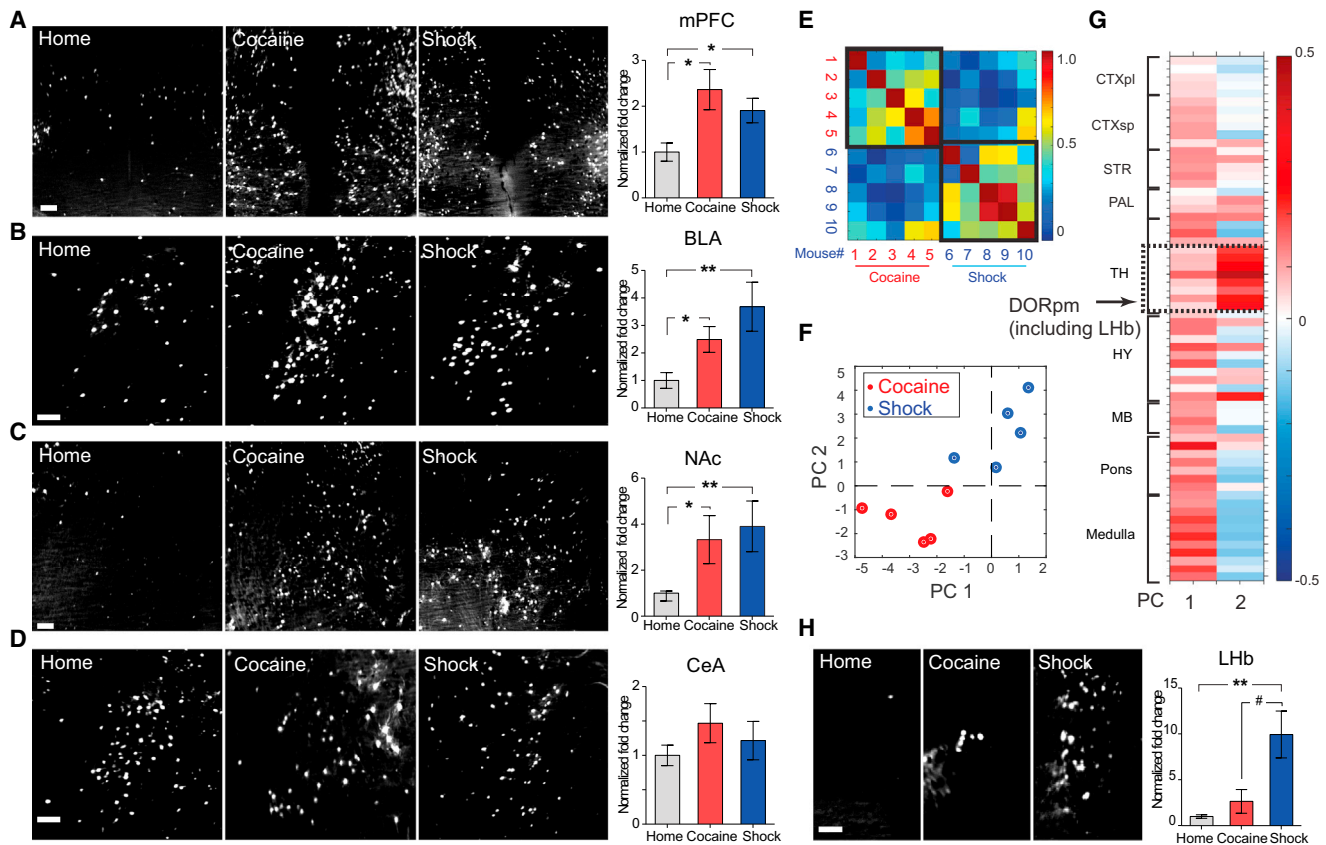
**Figure 2. Cocaine and Shock Recruit Overlapping Brain Regions**

(A–D) TRAP cells in manually annotated regions. Left: representative images taken at the center of the indicated regions (max-projection of 100 μm volume). Scale bars, 100 μm. Right: fold change in TRAP cell numbers (normalized to home cage).

(E) Pearson correlation among the ten mice, based on the r-value computed from fold-activation changes relative to home cage across all non-zero-containing brain regions. Note the higher brain-wide correlation values within behavioral groups (black bounding boxes) compared to across-groups.

(F) Locations of individual mice projected into the 2D space of the two principal components (PCs) comprising the majority of the variance (in arbitrary PC units), where the position of each mouse corresponds to the extent to which a particular principal component accounts for that mouse's variance across all brain regions.

(G) Principal component coefficients (in arbitrary PC weight units) across brain areas—the contribution of each brain area to each principal component—were summarized as clusters of proximal regions. Note the distinct region-selective contribution to PC 2 (dashed box; detailed in text). CTXpl/sp, cortical plate/subplate; SRT, striatum; PAL, pallidum; TH, thalamus; HY, hypothalamus; MB, midbrain; DORpm, polymodal association cortex-related dorsal thalamus.

(H) Representative image and quantification of TRAP cells in LHb. Scale bar, 100 μm. For all panels, n = 5 per group, *p < 0.05, **p < 0.01, unpaired t test comparing behavioral group to home cage; # p < 0.05, unpaired t test comparing cocaine versus shock group. All p values were adjusted for multiple comparisons using the false discovery rate method. Error bars, mean ± SEM.

See also Figure S2 and Table S1.

key capabilities achieved included much faster speed and lower cost, as well as automated analysis algorithms adapted to both TRAP labeling and widely available commercial light-sheet microscope hardware (Figures 1A, 1C, 1D, and S1E–S1H; see the Experimental Procedures).

Employing this integrated TRAP/CLARITY approach, multiple cohorts (with temporally delimited exposure to appetitive cocaine dosing, aversive foot shock, or neither experience; n = 5 mice per group) were processed using two-color imaging on the light-sheet microscope. Image volumes taken in the green (autofluorescence) channel were iteratively co-registered, using an intensity-based non-linear registration algorithm, to generate an average reference brain. The registration based on the green

channel from each brain was then used to warp the red channel (consisting of the TRAP signal) for each brain into this reference space (Figure S1I).

We first manually delineated potentially relevant regions in the reference brain, including mPFC, NAc (nucleus accumbens), BLA, BNST (bed nucleus of the stria terminalis), LH (lateral hypothalamus), PVN (paraventricular nucleus of hypothalamus), and CeA (central nucleus of the amygdala). At this level of inspection, the singly defined regional levels of neuronal activation were found to be largely similar between the two very different kinds of experience (Figures 2A–2D and S2H–S2J; Table S1), highlighting the need for a more refined analysis. To search for patterns in cell labeling that could differentiate the two

**Cell**

conditions despite this apparent similarity, we manually registered the Allen Brain Atlas (ABA) (Oh et al., 2014) to the CLARITY reference. Locations of experience-recruited cells were also mapped into the reference, so that the number of recruited cells in every brain region could be quantified in an unbiased fashion (Menegas et al., 2015); changes in TRAP cell numbers (relative to home cage-animal mean values) in ~200 brain regions were then automatically quantified (Figures S2A–S2G).

Individual single-region activation patterns consistent across subjects within a group largely agreed with the manual analysis. For example, robust increases in TRAPped cells were observed in both settings within mPFC, NAc, BLA, pallidal regions (containing BNST), and hypothalamus (Figure S2K). However, the change in active cell count across all regions revealed common multi-region correlation patterns in mice from the same experimental group, suggesting experience-specific brain-wide patterns (Figure 2E). To investigate these differences, we applied principal component analysis (PCA) to the matrix of activated cell-count changes in cocaine- or shock-labeled mice. The first two principal components (PCs) comprised >75% of the variance for the dataset (Figure S2L) and thus were examined more closely. Plotting the position of each mouse in the space defined by the first two PCs revealed a clear separation between the behavioral conditions (Figure 2F).

To better understand the source of this separation, we examined the PC loadings across all of the included brain areas (Figure 2G). The first PC was found to reflect more general differences in activated cell recruitment across all regions (e.g., higher mean change across all regions in shock versus control mice; p < 0.05, t test). The second PC, by contrast, revealed a specific correlated group of DORpm (polymodal association cortex-related dorsal thalamus) regions, containing the lateral habenula (LHb), a key nucleus for aversive behaviors (Li et al., 2011, 2013). These regions were more strongly recruited by shock than by cocaine, revealing a selective responsiveness to the aversive experience. Consistently, manual quantification also found that shock more than cocaine, activated the LHb (p < 0.01 for shock versus home-cage experience; p < 0.05 for shock versus cocaine experience; Figure 2H). Thus, this behavioral cohort-scale TRAP/CLARITY labeling revealed brain-wide patterns of neuronal activation, as well as quantitative region-specific activation differences at the cellular level between different experimental conditions.

### Resolving mPFC Populations and Projections Activated by Appetitive or Aversive Experience

Similarity in activation pattern by appetitive and aversive experiences has been reported in individually selected brain regions (verified broadly, though not in all regions, by the brain-wide analysis here) (Johnson et al., 2010; Xiu et al., 2014). A falsifiable hypothesis would be that the same neuron-type distribution was recruited by the two stimuli. In mPFC, the existing literature does not support or falsify this hypothesis, though mPFC is associated with specific reward and aversion processes (including cocaine-conditioned place preference, (Tzschentke and Schmidt, 1998, 1999), fear and anxiety behaviors (Burgos-Robles et al., 2009; Lammel et al., 2011; Shah et al., 2004; Shah and Treit, 2003), and more general functions poten-

tially relevant to the single-population hypothesis (including attention, salience- and novelty-detection, and working memory) (Dalley et al., 2004; Miller, 2000). The region-specific brain-wide analysis here may open the door to testing a distinct hypothesis—that appetitive and aversive experience recruit distinct neuron-type populations. Axonal projection anatomy is one of the most important features that might resolve principal cell population types involved in such distinct processes (Jennings et al., 2013; Kim et al., 2013; Lammel et al., 2012; Namburi et al., 2015), but this feature has been difficult to explore in a brain-wide fashion, while remaining linked (at the cellular level) to function during behavior.

A very strongly expressed activity-dependent cell-filling label (unlike traditional nuclear c-*fos* immunostaining or transiently or transgenically expressed fluorophores) in principle might allow for acquisition of this crucial wiring information as well from the same experimental subjects, provided that axon tracts of labeled neurons could be robustly imaged and quantified in this context. We therefore developed a CLARITY-optimized axonal-filling fluorescent protein, engineered, in part, by inserting the 3′ UTR of neuritin (NRN) RNA (Akten et al., 2011) at the C terminus of EYFP (Figures S3A and S3B). We found that this construct could be packaged into high-titer adeno-associated virus (AAV) capsids that indeed enabled focal injection-defined projection labeling in CLARITY; for example, efferent mPFC projections could be readily followed throughout the entire adult mouse brain after a single stereotaxic injection (Figures 3A and 3B). Visualizing axonal tracks in 3D revealed key topographical features that were difficult, if not impossible, to detect in thin 2D sections (Figures 3A and S3C); for example, a prominent axon bundle traveling from mPFC to ventral medial thalamus was observed to carry out a sharp U turn near the VTA (Figures 3C and 3D), a potentially important feature that has not been described in existing atlases (Figure S3D).

Quantifying these tracts was also an unresolved challenge, and we therefore developed a method to compute 3D structure tensors from CLARITY images for tractography (Figures S3E–S3H). Faithful reconstruction of calculated streamlines was achieved (using tools adapted from diffusion tractography; Supplemental Experimental Procedures); these streamlines mapped onto fibers from CLARITY images (Figures 3E and 3F), and importantly, the streamline count in each bundle tightly correlated with the ground-truth physical diameter of the axonal bundles (Figure S3I). Using this method, we reconstructed whole-brain projections based on CLARITY images (Figure 3G); connectivity between a seed region (defined by stereotaxic injection site) and any specified target could be readily visualized and assessed by counting streamlines (Figures 3H and S3J–S3M).

To integrate this capability, with the needed additional capability of projection-labeling in cells defined by their use during experience, we sought to develop a viral CreER/4TM strategy to translate time-locked activity to sustained transgene expression. We therefore engineered a c-Fos promoter combining minimal promoter and regulatory elements in intron-1 (Figure S4A) (Barth et al., 2004; Schilling et al., 1991; Smeyne et al., 1992) that can be packaged into AAV particles and is specific enough to capture neuronal activity (Figures S4B–S4D). We also inserted a destabilized ER-Cre-ER-PEST

**Cell**
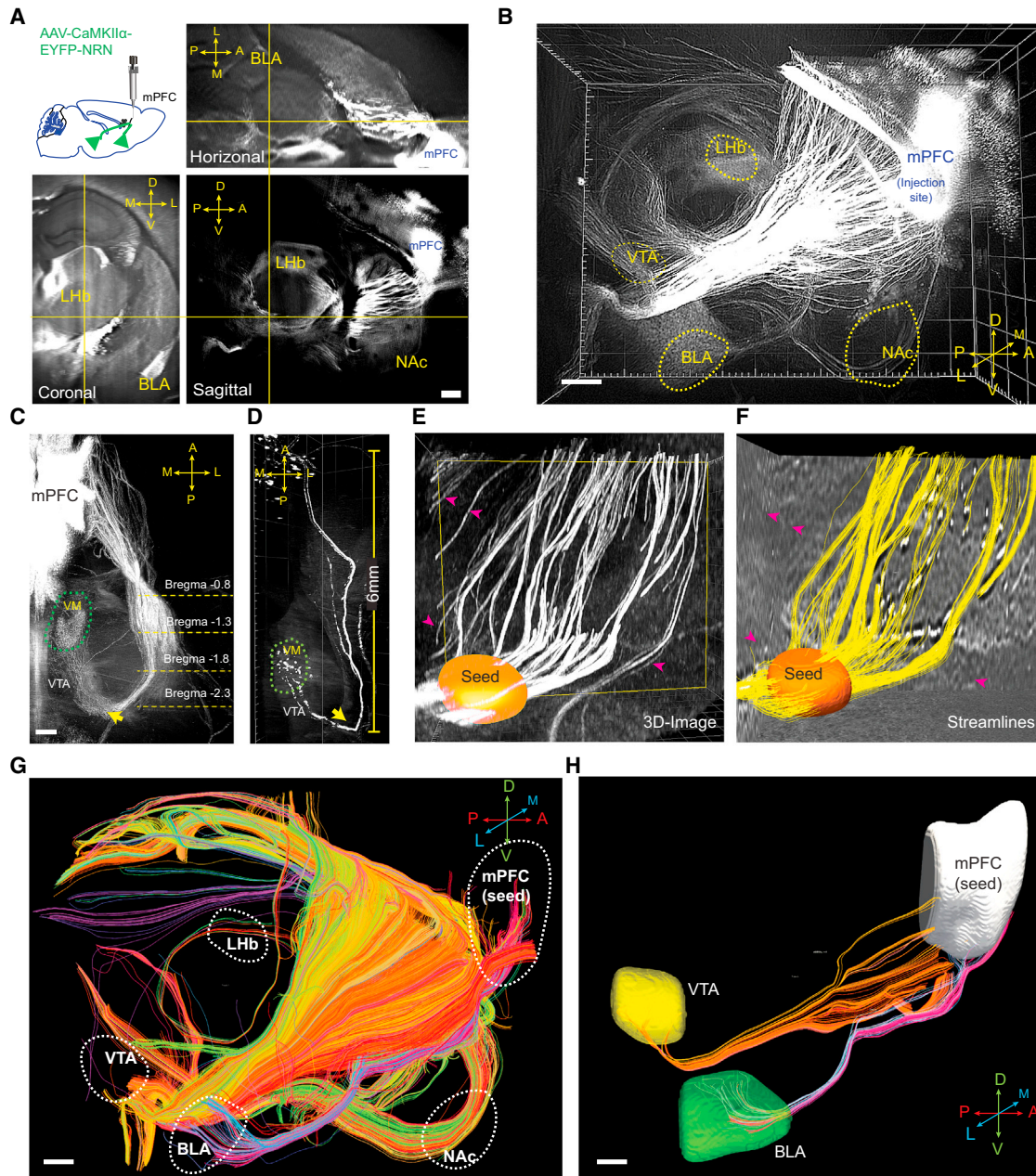


**Figure 3. CLARITY Enables Brain-wide Origin/Target-Defined Projection Mapping**

(A) 2D orthogonal views of a mouse brain. Insert shows schematic for location of viral injection. D, dorsal; V, ventral; A, anterior; P, posterior; L, lateral; M, medial.

(B) 3D rendering of CLARITY hemisphere, visualizing outgoing mPFC projections (imaged by 2× objective at 0.8× zoom with a single FOV, step size: 4 μm, 1,000 steps).

(C) 3D visualization of the axonal bundle projecting from mPFC to VM (ventral medial thalamus), showing tracts turning near the VTA (indicated by arrows).

(D) Visualizing the same projection in (C) with sparse labeling by injecting a smaller volume of the same virus (25 nL).

(E) Raw image from a CLARITY volume. Orange: user-defined "seed region" so that only the fibers passing this region were tracked.

(F) Streamlines reconstructed from (E), using structural tensor-based tractography. Note that fibers in the CLARITY image that did not pass the user-defined seed region were excluded in the reconstruction (indicated by the magenta arrows).

(G) Reconstructed brain-wide streamlines from CLARITY image in (B). The streamlines are color-coded for orientation. A-P, red; D-V, green; L-M, blue.

(H) Representative computational isolation of mPFC fibers that project to VTA (yellow) or BLA (green).

Scale bars, 500 μm.

See also Figure S3.
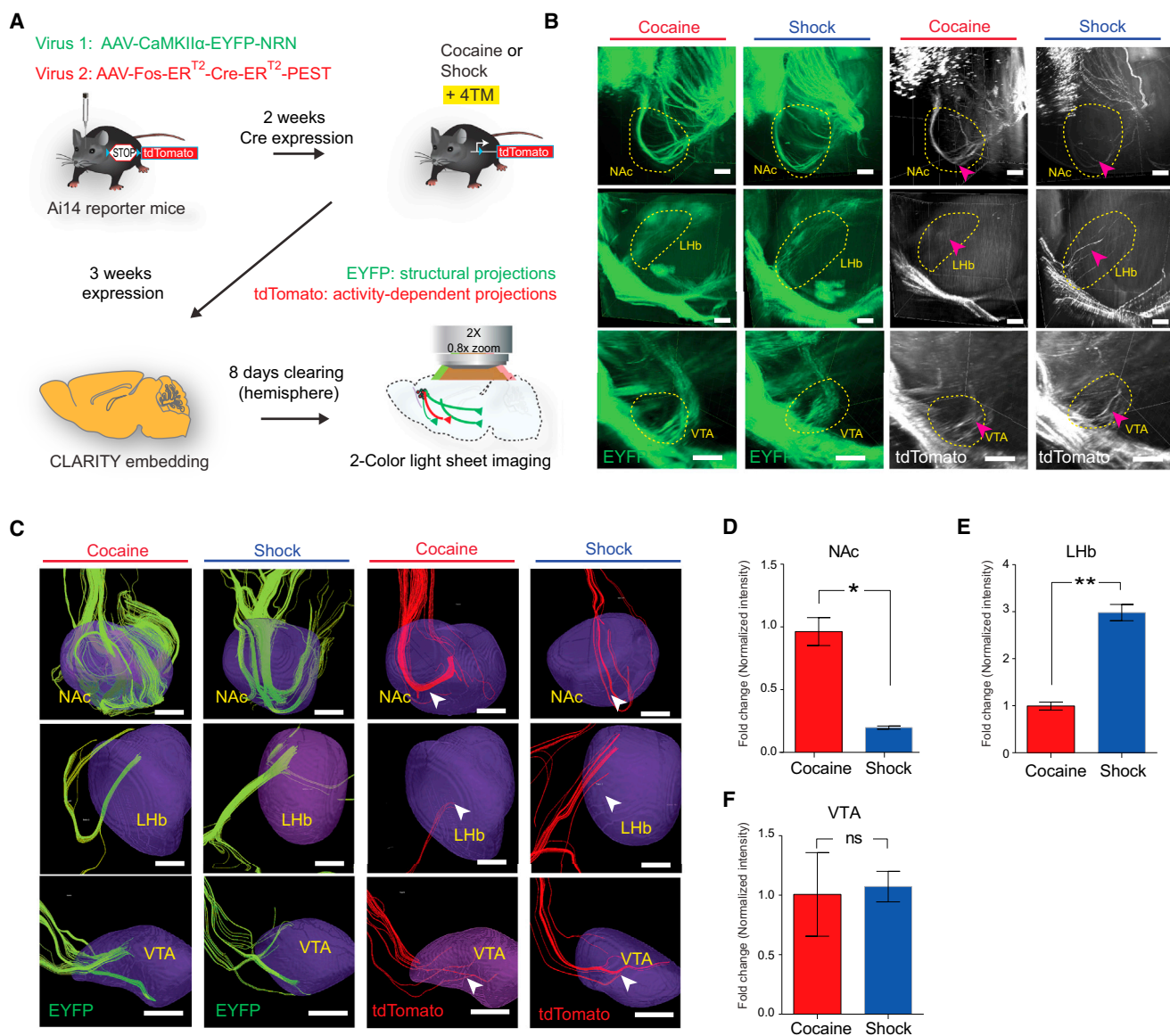
**Figure 4. Distinct Projection Targets of Cocaine and Shock-Activated mPFC Populations**

(A) Summary of CAPTURE workflow (described in text).

(B) Representative CLARITY images of the structural projections (green, EYFP) and activity-dependent projections (white, tdTomato) from cocaine- and shock-labeled mice in NAc (top), LHb (middle), and VTA (bottom). Arrowheads indicate axon bundles terminating in the circled region. Scale bar, 200 μm.

(C) Reconstructed streamlines from (B), showing streamlines terminating in the 3D brain regions (purple). Green streamlines, reconstructed from EYFP fibers; red streamlines, reconstructed from tdTomato fibers. Scale bars, 200 μm.

(D–F) Quantification of projection intensity from cocaine- and shock-activated mPFC populations in three regions. Behavior-specific projection intensity was quantified using the ratio between red and green fibers (i.e., the number of red streamlines, divided by the number of green streamlines) terminating in indicated regions and plotted as fold change (relative to the cocaine group, n = 6 per group; ns, p > 0.05, *p < 0.05, **p < 0.01, unpaired t test). Error bars, mean ± SEM. See also Figure S4.

cassette under this promoter (Kawashima et al., 2013; Li et al., 1998; Matsuda and Cepko, 2007); when injected into a reporter mouse, this viral CreER/4TM system reliably enabled activity- and tamoxifen-dependent cell-body and projection labeling (Figures S4E and S4F).

A final essential feature for quantitative activity-dependent projection mapping was normalization on an individual level to

the absolute tract labeling strength independent of activity; this normalization is crucial in a virus-based approach to control for variation in injection efficacy. We enabled this feature (Figure 4A) by building in simultaneous two-color activity-independent (structural, EYFP) labeling and activity-dependent (tdTomato) labeling of projections from the same injection site, in which these two viruses infected cells with a stable relative ratio across

animals (Figures S4G and S4H). Dual-color quantification of projections to multiple downstream regions is then achieved by counting the number of streamlines ending in these regions, and the activity-dependence is corrected for anatomical and injection variability from the red/green streamline ratio at the individual animal level. This quantification of projection use across the brain from behaviorally defined neuronal populations is (for brevity) termed here CLARITY-based activity projection tracking upon recombination, or CAPTURE (Figure 4A).

### Distinct Projection Patterns among Behavioral Experience-Defined mPFC Populations

We applied CAPTURE to quantify projections from cocaine- and shock-recruited mPFC populations. Ai14 reporter mice were co-injected with CaMKIIα-EYFP-NRN and cFos-ER-Cre-ER-PEST AAVs and subjected to 4TM-mediated cocaine and shock labeling. With CAPTURE, projections from all CaMKIIα (principally excitatory glutamatergic) neurons are labeled with EYFP and projections from behaviorally recruited populations are labeled with tdTomato. Importantly, EYFP fibers in the NAc, BLA, and VTA were found to be indistinguishable between the cocaine- and shock-labeled animals, indicating minimal variation in viral injection, transduction, and expression between the two groups (Figure 4B).

In the very same animals, significantly more projections from behaviorally activated mPFC neurons were observed targeting the NAc in cocaine-exposed animals compared to shock-exposed animals. Conversely, we observed significantly more behaviorally activated mPFC fibers to the LHb in shock-exposed animals (Figures 4C–4F). No significant difference in red/green (activity/structure) ratio was observed between the two groups in the VTA, showing no detectable systematic difference in efficiency or targeting of viral labeling. The cocaine-activated mPFC population thus preferentially projects to the NAc, whereas the shock-activated population projects more strongly to LHb, revealing that the neurons recruited in mPFC by distinct-valence experience are not simply different in terms of the patterns of input that they happen to receive, but represent anatomically distinct cell populations in terms of projection pattern across the brain.

### Molecular Signature of Experience-Defined mPFC Neurons: Pre-existing NPAS4 Population

Next, we sought to identify molecular distinctions among cocaine- and shock-responsive populations in mPFC. We began by crossing Arc^CreER mice to a Cre-dependent ribosome-tagged mouse (Long et al., 2014) to allow for labeling the ribosomes from neuronal populations activated by well-defined stimuli (Figure 5A). With this approach, the tagged ribosome can be immunoprecipitated (IP) from tissue lysate using an anti-GFP antibody, isolating translating mRNA for analysis (Ekstrand et al., 2014; Heiman et al., 2008; Sanz et al., 2009). These mice were exposed to either cocaine or shocks with 4TM. After labeling, mice were returned to the home cage for 2 weeks before initiation of ribosome purification, a design focused on identifying intrinsic signatures of these populations rather than on immediate mRNA expression changes associated with the exposure to stimuli.

Equal enrichment of GFP transcripts under these conditions was first confirmed by qPCR (Figure S5A). Four groups of mRNA ("IP fraction" for ribosome-associated transcripts from cocaine and shock and "input" for whole-tissue lysate from cocaine and shock; see the Experimental Procedures) were then analyzed by microarray. For both stimuli, IP fraction groups were enriched 3-fold in the ribosomal-component mRNA (Rpl10a) compared with input groups (Figures 5C and 5D), further demonstrating similar levels of mRNA enrichment between treatments. Gene expression profiles from cells recruited under the two conditions were highly similar upon initial examination (<10 genes showed >2-fold difference; Figure S5C); however, a transcript of the activity-dependent transcription factor Npas4 (Bloodgood et al., 2013; Lin et al., 2008; Shamloo et al., 2006) was uniquely enriched in cocaine-activated cells compared to shock-activated cells (Figure 5B). This enrichment was confirmed by comparing the IP fraction to the input from the cocaine-labeled cells (Figure 5C) and finally validated by qPCR (Figure 5E); in contrast, this enrichment was not observed by comparing the IP and input fractions from the shock-labeled population (Figure 5D).

Because Npas4 itself is an immediate early gene that can be transiently induced by neuronal activity, we first tested if its enrichment in the cocaine-recruited population could relate to a lasting general cocaine-elevated Npas4 transcription. Both cocaine and shock caused a rapid increase of Npas4 expression in mPFC within 30 min, as expected; however, this induction under both conditions, (also as expected) completely returned to baseline after 10 days before the ribosome was profiled (Figure S5B). Indeed, no difference was observed when we examined Npas4 expression in whole-tissue lysates from cocaine- and shock-labeled mPFC (Figure 5E), indicating that exposure to cocaine did not lead to an overall long-term increase of Npas4 expression in mPFC.

At the single-cell level, we discovered that the number of mPFC cells with NPAS4 immunoreactivity did not differ between behavioral groups or between the home-cage and behavior-challenged animals (Figures 5F–5H). However, TRAP/NPAS4 double-positive cell counts were significantly higher in cocaine-exposed mice (Figure 5I), consistent with activity recruitment of an NPAS4 population. Similarly, the percentage of NPAS4+ cells among TRAP+ cells was also significantly higher in cocaine-labeled mPFC than in shock-labeled mPFC (Figure 5J). Importantly, we found that another positive-valence experience (highly palatable food consumption), but not another negative-valence experience (restraint stress), also selectively recruited this mPFC NPAS4+ population (Figures S5D and S5E), further illustrating that a pre-existing NPAS4+ population is preferentially activated by salient stimuli associated with positive valence rather than negative valence. Finally, the molecular overlap between the positive valence-associated population and the NPAS4+ population led us to further examine the spatial distribution of valence-specific populations, since the NPAS4+ cells appeared to be enriched in superficial layers of the mPFC (Figures 5F and S5E); indeed, the positive-valence experiences were associated with a significantly larger fraction of TRAPped layer 2/3 neurons in the mPFC than in the negative-valence experiences (Figure S5F).

**Cell**
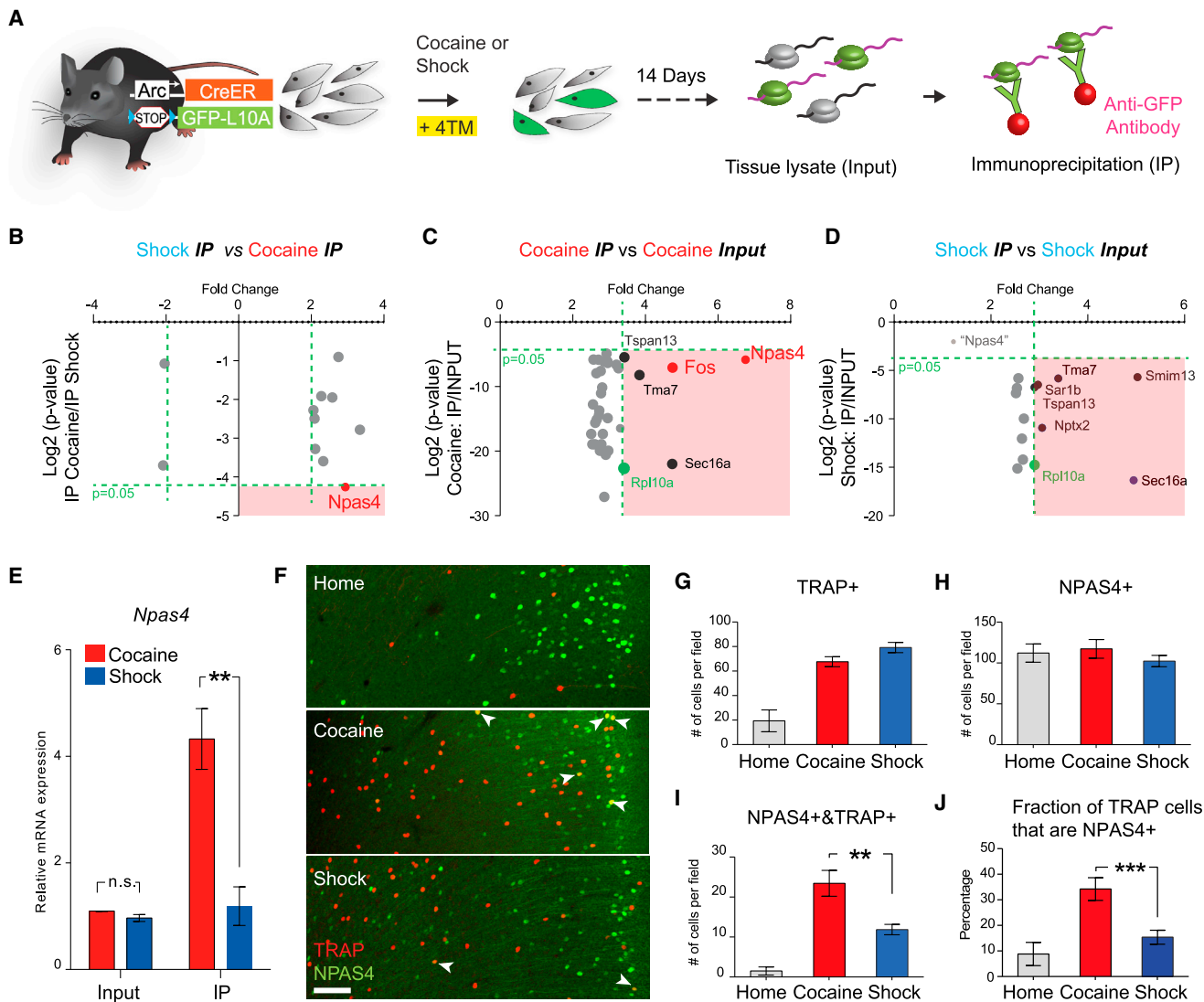


**Figure 5. Cocaine Preferentially Activates the NPAS4+ Population in mPFC**

(A) Schematic of activity-dependent ribosome profiling. Green, activated neurons; gray, non-activated neurons.

(B–D) Scatter plot of the most-enriched genes comparing cocaine- versus shock-activated cells (cocaine IP versus shock IP) (B), cocaine IP versus cocaine input (C) and shock IP versus shock input (D). The bottom right quadrant (pink) of each scatter plot denotes genes with p < 0.05 and fold change >2 for the indicated comparisons. As a positive control, the enrichment of RpL10a is highlighted in green. Black dots denote genes that were non-specifically enriched by IP (as shown enrichment in both cocaine and shock IP fraction). In (D), Npas4 (light-gray dot, fold change = 1.35, p value = 0.385) did not approach the statistically significant (pink) quadrant.

(E) Quantitative PCR analysis of *Npas4* mRNA expression in the input and IP fractions.

(F) Representative images showing the overlap between TRAP+ and NPAS4+ cells in the mPFC. Scale bar, 100 μm. Arrowheads indicate double-positive cells.

(G–I) Quantification of numbers of TRAP+ (G), NPAS4+ (H), and TRAP+&NPAS4+ (I) cells in the mPFC.

(J) Percentage of NPAS4+ cells in TRAP+ cells under three conditions. n = 4 per group, *p < 0.05, **p < 0.01, unpaired t test. Error bars, mean ± SEM.

See also Figure S5 and Movie S1.

## Cocaine- and Shock-Activated Populations Control Appetitive and Aversive Behaviors

Next, we tested if electrical activity in these behavioral activity-defined populations had distinct positive or negative conditioning valence for the same animals that had experienced the stimulus, assessed by causal impact on behavior during the place

preference task. To maintain robust, low-background, and direct region-specific control in mPFC, we designed a viral approach employing channelrhodopsin tagged with EYFP (ChR2-EYFP) under the control of the AAV-cFos backbone described earlier (termed fosCh; Figure 4A). Animals injected with this virus (in mPFC) were exposed to daily cocaine dosing or shock over 5
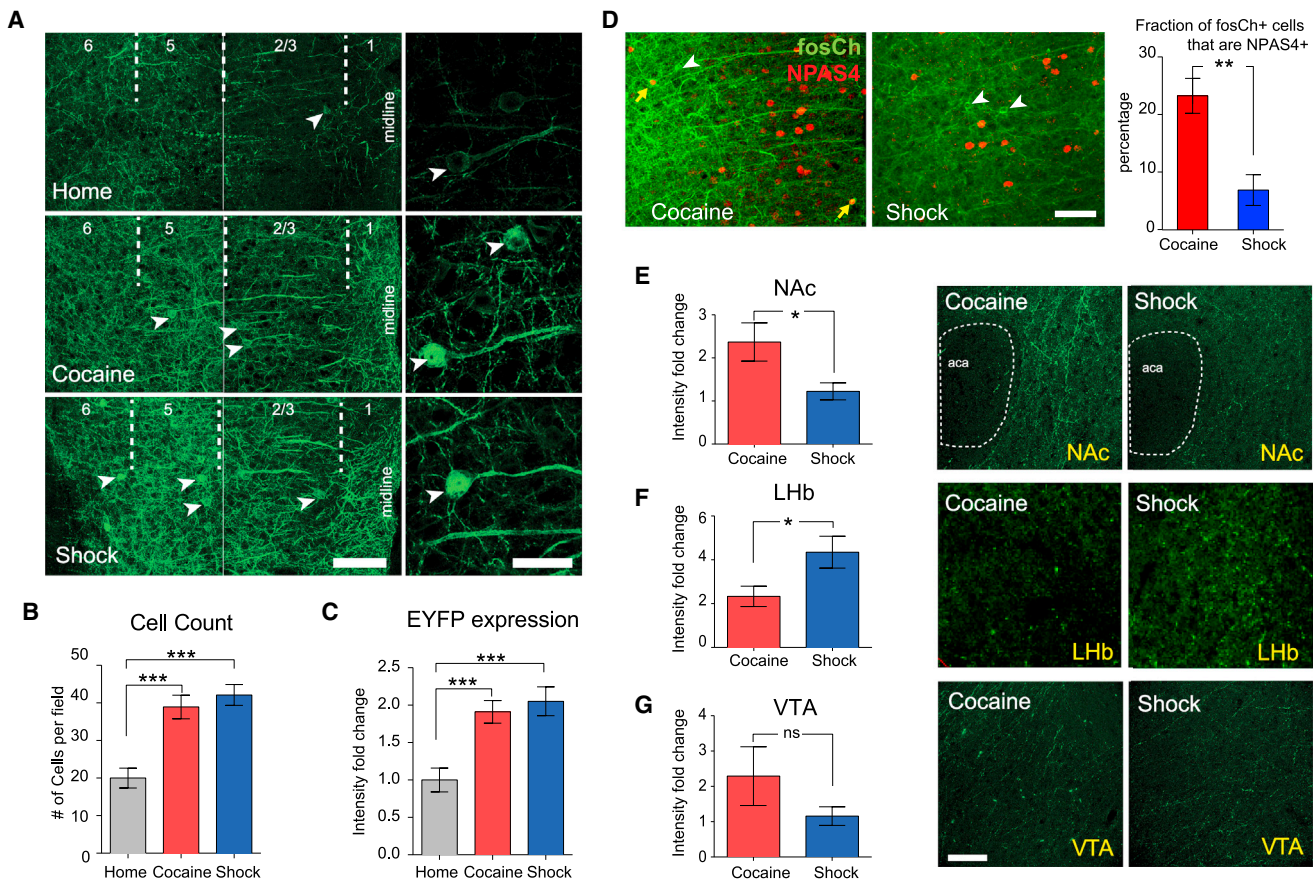
**Figure 6. Use of fosCh for Targeting Cocaine- and Shock-Activated mPFC Populations**

(A) Representative images showing fosCh expression in mPFC following the indicated behaviors. Left, two 40× images were stitched for visualizing lamina across the cortical depth. Arrowheads indicate fosCh+ neurons. Scale bars, 100 μm. Right, high-magnification images of individual fosCh neurons. Scale bars, 25 μm.

(B) Fold change in fosCh cell numbers.

(C) Fold change in mean EYFP fluorescence intensity. n = 11–14 per group, ***p < 0.001, unpaired t test.

(D) Representative images and quantification of fosCh and NPAS4+ cells. White arrowheads indicate fosCh-positive neurons. Yellow arrows indicate NPAS4/ fosCh double-positive cells. n = 5 per group, **p < 0.01, unpaired t test.

(E–G) Left: comparing density of fosCh projections for cocaine and shock groups. Right: representative images showing the density of fosCh projections in indicated regions. aca, anterior part of anterior commissure. Scale bars, 100 μm. n = 11–14 per group, *p < 0.05, unpaired t test. Error bars, mean ± SEM.

See also Figure S6.

consecutive days, after which time robust increases in the number of fosCh-labeled cells and in EYFP expression were observed (Figure 6A–6C).

We first quantified *Npas4* expression in fosCh cells, hypothesizing that cocaine-labeled fosCh cells would exhibit higher *Npas4* expression compared with shock-labeled fosCh cells. This was indeed the case (Figure 6D); importantly, expression of general excitatory or inhibitory neuronal markers did not differ between those two populations (Figures S6A and S6B). Consistent with CAPTURE findings, cocaine-labeled fosCh cells were found to project strongly to NAc, while the LHb contained significantly denser fibers arising from the shock-labeled cells (Figures 6E–6G). Crucially, this method of targeting was sufficient to enable optical control over the resulting sparsely distributed neuronal subsets; fosCh-labeled cells displayed robust light-evoked firing assessed by in vivo electrophysiological recording (Figures 7A and 7B). Together, these data demonstrated resolu-

tion with the fosCh strategy of the same pattern that had been characterized molecularly and anatomically and enabled the final test of whether these neuronal subsets were capable of differentially controlling behavior.

To address this question, we employed the real-time place preference paradigm in which 10 Hz light-pulse trains were automatically triggered on entry into one side of a behavioral chamber. Place preference was monitored over three consecutive trials: before, during, and after light delivery for reactivation of fosCh-defined neuronal ensembles (Figure 7C). To control for the possibility that behavior could be biased by randomly labeled neurons, an additional group of animals was included in which comparable expression of ChR2 was driven by the CaMKIIα promoter without link to prior activity (Figures S7A and S7B). Optogenetic stimulation of these non-activity-specific neuronal populations did not influence place preference, nor were homecage-recruited fosCh-population animals observed

**Cell**
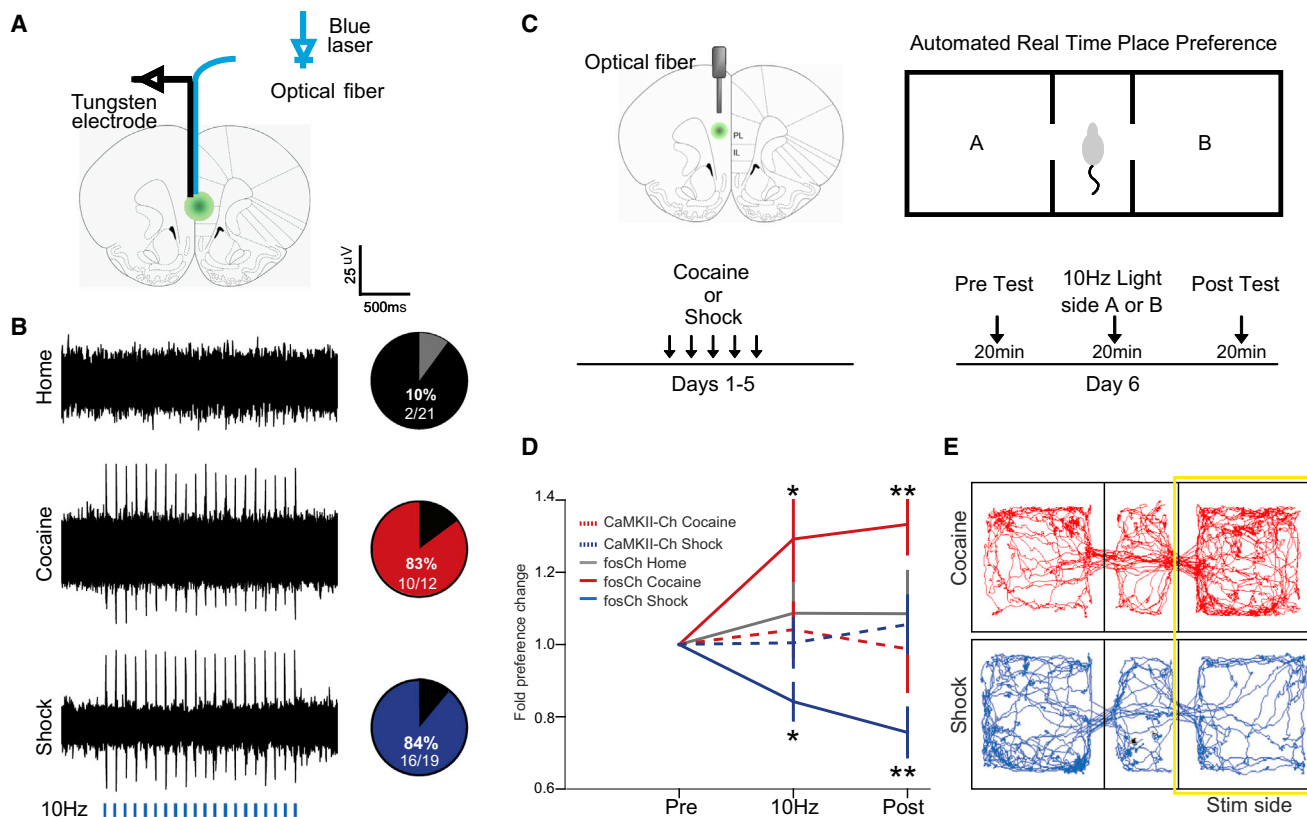


**Figure 7. Differential Behavioral Influence of Cocaine- and Shock-Activated mPFC Populations**

(A) Schematic to illustrate the placement of the recording electrode and optical fiber for in vivo recording. The optrode was lowered in 100 μm steps along the dorsal-ventral axis of mPFC.

(B) Left: representative extracellular recordings showing neural response to a 10 Hz light train (5 ms pulses for 2 s, every 5 s, 5 mW 473 nm light, indicated by blue bars). Right: pie charts indicate percentage of recording sites showing light-evoked action potential firing for the home cage (gray), cocaine (red), and shock (blue) groups.

(C) Schematic shows the location of the optical fiber positioned above the injection site in green. After 5 days of training, mice were tested by a real time place preference test, which consisted of three consecutive 20-min trials.

(D) Behavioral results plotted as fold change in preference for the light stimulated side (normalized by baseline preference) across each of the trials. n = 10–14 per group, *p < 0.05, **p < 0.01, ANOVA, followed by Tukey's multiple comparison test. Error bars, mean ± SEM.

(E) Movement tracking data from representative cocaine- and shock-labeled animals during the light-stimulation trial.

See also Figure S7.

to exhibit preference or aversion for the chamber in which the cells were optically activated. Remarkably, however, reactivation of the shock- or cocaine-defined fosCh populations induced significant (and opposite-direction) shifts in place preference, with cocaine-exposed mice demonstrating preference, and shock-exposed mice demonstrating aversion, for the photostimulation-paired side (Figures 7D and 7E; mean preference change at post-test for cocaine: 1.3x ± 0.1, Wilcoxon p = 0.0006; for shock: 0.8x ± 0.1, Wilcoxon p = 0.002). These data reveal that the activity-defined mPFC neural populations differ not only anatomically and molecularly but also in functional impact in modulating behavior.

## DISCUSSION

It has been remarked (building on Dobzhansky's comment that "nothing in biology makes sense except in the light of evolution"

(Dobzhansky, 1973) that "nothing in neurobiology makes sense except in the light of behavior" (Shepherd, 1988). This perspective may be directly relevant to efforts in multiple subfields of neuroscience to describe the cellular diversity in nervous systems. While these efforts are pioneering and informative, it may be limiting to collect cellular typology datastreams relating to anatomy, genetics, and membrane biophysics, without knowledge of the importance of activity patterns in those same cells during behavior. However, forging such direct linkages has been difficult, especially in vertebrates. Indeed no system may be more challenging in this regard than the mammalian mPFC, which does not have well-defined direct sensory input or motor output pathways, and wherein principal cells with similar spike properties and anatomical positioning exhibit divergent or even opposing responses during behavior. Here, we have addressed these challenges, focusing on the specific problem of whether mPFC cells that respond differently to positive or negative

valence experiences are, in fact, separable cell types as definable by molecular or anatomical measures, as well as by causal impact on behavior.

We identified not only brain-wide projection patterns separating mPFC cells responding to positive- and negative-valence experience but also a unique and unexpected enrichment of NPAS4 expression characteristic of mPFC cells responding to appetitive experience (Figure 4; Movie S1) that was not observed in cells responding to salient aversive experiences with comparable conditioning value. In illustrating that a pre-existing NPAS4+ population is preferentially activated by salient stimuli associated with positive valence rather than with negative valence, these mPFC results may be contrasted with elegant memory-engram models in which cells expressing a key activity marker may be recruited into diverse stimulus representations, as with CREB-expressing cells in amygdala fear conditioning (Han et al., 2007). NPAS4 has been linked to cellular and microcircuit processes relating to the balance of excitation and inhibition, including a form of adaptive plasticity in which inhibitory synapses are formed on cells in response to high levels of excitation (Bloodgood et al., 2013; Lin et al., 2008; Maya-Vetencourt et al., 2012; Spiegel et al., 2014). This previously known role of NPAS4, together with the observation here that the positive-valence, but not negative-valence, experience recruited the mPFC NPAS4 population may bear relevance to previous observations among behaviorists that appetitive-learning experiences may be more vulnerable to adaptation or extinction, whether with natural stimuli or in pathological situations seen in drug dependence (Bouton, 2004).

The CAPTURE approach (the integration of enhanced CLARITY for behavioral cohort-scale work with cell and projection quantification linked to activity during behavior) is provided here in the form of tools, software, and datasets that may be readily applied across systems. The intact-brain approach is not only scalable in a practical manner to include large cohorts of experimental subjects and enabling of quantitative projection and population analysis but also helps address key confounds relating to selection bias and loss of continuity in traditional sectioning approaches widely used across neuroscience and biology. Moreover, improved 3D understanding of the path of behaviorally relevant axon bundles through the intact brain may be critical for the expanding field of neuromodulation, which is increasingly dependent on accurate targeting of white matter tracts (Henderson, 2012).

These tools are also readily adaptable for broader applications. For example, the NRN construct allowing rapid axonal projection labeling may be useful along with recombinase- or tetracycline-controlled (Liu et al., 2012) promoters for driving axon-filling fluorophores in approaches to multiplexed cell-type-specific CLARITY projection mapping or for driving opsins (Gore et al., 2015) to enhance functional assays of long-range projections (for example, to test synaptic release at different points along an axonal projection in slice assays or to test behavioral significance of cells defined by projection target). The fos-CreER virus (Figure 4) might be used in conjunction with future generations of high-potency opsin expression systems to enable optogenetic control based on experience temporally defined with 4TM, in strategies that could be eventually developed to reduce the number of repeated exposures currently required for sustained expression using the fosCh construct (Figure 7C). Lastly, recombinase-dependent constructs expressing $Ca^{2+}$ indicators (such as G/RCaMPs) may be used to resolve temporal dynamics and individual-neuron activity magnitudes within experience-defined cells; these features are not accessible by conventional binary IEG-based methods but may be important, for example, in positive versus negative reinforcement in the PFC (Pi et al., 2013; Pinto and Dan, 2015).

In future work, it will be important to build on these results with additional investigation of the mPFC populations. For example, exploring long-term changes in gene expression and structural properties in these assemblies after experience (continuing to leverage the activity-tagging and intact-brain methods) may help to identify cell-population-resolved processes important in plasticity of adaptive or maladaptive circuit dynamics. And identification of these separable mPFC populations, along with analysis of their interactions and modulations during adaptive and pathological conditions (in the setting of rapid parallel advances in high-content molecular phenotyping, targeted drug screening and design, and genome editing) may point the way toward cell-population-targeted interventions in diseases of addiction, anxiety, and fear.

## EXPERIMENTAL PROCEDURES

### Animals

Male and female C57BL/6J mice were group-housed on a reverse 12-hr light/dark cycle. Mice were 6–8 weeks old at viral infusion. Ai14 and wild-type C57BL/6 mice were purchased from JAX. Rosa26loxp-stop-loxp-eGFP-L10 mice were from Dr. Evan Rosen at Harvard Medical School. Male mice were used in behavioral assays. Both male and female mice were used for anatomy assays. All experimental protocols were approved by the Stanford University Institutional Animal Care and Use Committee and were in accordance with the guidelines from the NIH.

### CAPTURE Labeling

Ai14 mice were injected with a 1-μl mixture of AAV8-CaMKIIα-EYFP-NRN and AAV8-cFos-ER-Cre-ER-PEST in the mPFC. 2 weeks later, the mice were given 15 mg/kg cocaine (IP) or 20 random foot shocks (2 s/0.5 mA, two shocks/minute on average) for 2 consecutive days. The control group remained in their home cage for the whole period. 10 mg/kg 4-TM was given to all mice 3 hr after the last behavior section to enable CreER-mediated recombination. The mice were returned to their home cages for an additional 4 weeks to allow the full expression of fluorophores.

### CLARITY and Whole-Brain Imaging

Three key features of the new CLARITY platform were (1) accelerated clarification through parallelized flow-assisted clearing crucial for large cohorts and independent of specialized equipment, such as electrophoresis or perfusion chambers, (2) >90% cost reduction using a new refractive index-matching process, and (3) optical properties such that the whole mouse brain can be imaged using a commercial light-sheet microscope (Lavision) under a single field of view and as a single stack in less than 2 hr with single-cell resolution (this speed and simplicity is also useful for large behavioral cohorts). The COLM system (described earlier in Tomer et al., 2014; Lerner et al., 2015) is optimized for high-resolution imaging and is most useful for studies requiring sub-cellular information, while the approach outlined here is optimized for speed and practicality in cellular resolution work, most useful for robust application to large cohorts in CLARITY (see the Supplemental Experimental Procedures). All custom software, including the scripts used for atlas building, registration, and analysis, as well as code for CLARITY-based tractography, are freely available in a unified package at http://capture-clarity.org. The Web

**Cell**

site also provides detailed protocols, sample images, and other CLARITY-related resources.

## SUPPLEMENTAL INFORMATION

Supplemental Information includes Supplemental Experimental Procedures, seven figures, one table, one movie, and one data file and can be found with this article online at http://dx.doi.org/10.1016/j.cell.2016.05.010.

## AUTHOR CONTRIBUTIONS

## ACKNOWLEDGMENTS

## REFERENCES

Akten, B., Kye, M.J., Hao, T., Wertz, M.H., Singh, S., Nie, D., Huang, J., Merianda, T.T., Twiss, J.L., Beattie, C.E., et al. (2011). Interaction of survival of motor neuron (SMN) and HuD proteins with mRNA cpg15 rescues motor neuron axonal deficits. Proc. Natl. Acad. Sci. USA 108, 10337–10342.

Barth, A.L., Gerkin, R.C., and Dean, K.L. (2004). Alteration of neuronal firing properties after in vivo experience in a FosGFP transgenic mouse. J. Neurosci. 24, 6466–6475.

Bloodgood, B.L., Sharma, N., Browne, H.A., Trepman, A.Z., and Greenberg, M.E. (2013). The activity-dependent transcription factor NPAS4 regulates domain-specific inhibition. Nature 503, 121–125.

Bouton, M.E. (2004). Context and behavioral processes in extinction. Learn. Mem. 11, 485–494.

Burgos-Robles, A., Vidal-Gonzalez, I., and Quirk, G.J. (2009). Sustained conditioned responses in prelimbic prefrontal neurons are correlated with fear expression and extinction failure. J. Neurosci. 29, 8474–8482.

Chung, K., Wallace, J., Kim, S.Y., Kalyanasundaram, S., Andalman, A.S., Davidson, T.J., Mirzabekov, J.J., Zalocusky, K.A., Mattis, J., Denisin, A.K., et al. (2013). Structural and molecular interrogation of intact biological systems. Nature 497, 332–337.

Dalley, J.W., Cardinal, R.N., and Robbins, T.W. (2004). Prefrontal executive and cognitive functions in rodents: neural and neurochemical substrates. Neurosci. Biobehav. Rev. 28, 771–784.

Dobzhansky, T. (1973). Nothing in biology makes sense except in the light of evolution. Am. Biol. Teach. 35, 125–129.

Ekstrand, M.I., Nectow, A.R., Knight, Z.A., Latcha, K.N., Pomeranz, L.E., and Friedman, J.M. (2014). Molecular profiling of neurons based on connectivity. Cell 157, 1230–1242.

Gore, F., Schwartz, E.C., Brangers, B.C., Aladi, S., Stujenske, J.M., Likhtik, E., Russo, M.J., Gordon, J.A., Salzman, C.D., and Axel, R. (2015). Neural representations of unconditioned stimuli in basolateral amygdala mediate innate and learned responses. Cell 162, 134–145.

Guenthner, C.J., Miyamichi, K., Yang, H.H., Heller, H.C., and Luo, L. (2013). Permanent genetic access to transiently active neurons via TRAP: targeted recombination in active populations. Neuron 78, 773–784.

Han, J.H., Kushner, S.A., Yiu, A.P., Cole, C.J., Matynia, A., Brown, R.A., Neve, R.L., Guzowski, J.F., Silva, A.J., and Josselyn, S.A. (2007). Neuronal competition and selection during memory formation. Science 316, 457–460.

Hayden, B.Y., Nair, A.C., McCoy, A.N., and Platt, M.L. (2008). Posterior cingulate cortex mediates outcome-contingent allocation of behavior. Neuron 60, 19–25.

Heiman, M., Schaefer, A., Gong, S., Peterson, J.D., Day, M., Ramsey, K.E., Suárez-Fariñas, M., Schwarz, C., Stephan, D.A., Surmeier, D.J., et al. (2008). A translational profiling approach for the molecular characterization of CNS cell types. Cell 135, 738–748.

Henderson, J.M. (2012). "Connectomic surgery": diffusion tensor imaging (DTI) tractography as a targeting modality for surgical modulation of neural networks. Front. Integr. Nuerosci. 6, 15.

Hof, P.R., Ungerleider, L.G., Webster, M.J., Gattass, R., Adams, M.M., Sailstad, C.A., and Morrison, J.H. (1996). Neurofilament protein is differentially distributed in subpopulations of corticocortical projection neurons in the macaque monkey visual pathways. J. Comp. Neurol. 376, 112–127.

Hsiang, H.L., Epp, J.R., van den Oever, M.C., Yan, C., Rashid, A.J., Insel, N., Ye, L., Niibori, Y., Deisseroth, K., Frankland, P.W., and Josselyn, S.A. (2014). Manipulating a "cocaine engram" in mice. J. Neurosci. 34, 14115–14127.

Insel, N., and Barnes, C.A. (2015). Differential activation of fast-spiking and regular-firing neuron populations during movement and reward in the dorsal medial frontal cortex. Cereb. Cortex 25, 2631–2647.

Ito, S., Stuphorn, V., Brown, J.W., and Schall, J.D. (2003). Performance monitoring by the anterior cingulate cortex during saccade countermanding. Science 302, 120–122.

Jennings, J.H., Sparta, D.R., Stamatakis, A.M., Ung, R.L., Pleil, K.E., Kash, T.L., and Stuber, G.D. (2013). Distinct extended amygdala circuits for divergent motivational states. Nature 496, 224–228.

Johnson, Z.V., Revis, A.A., Burdick, M.A., and Rhodes, J.S. (2010). A similar pattern of neuronal Fos activation in 10 brain regions following exposure to reward- or aversion-associated contextual cues in mice. Physiol. Behav. 99, 412–418.

Kawashima, T., Kitamura, K., Suzuki, K., Nonaka, M., Kamijo, S., Takemoto-Kimura, S., Kano, M., Okuno, H., Ohki, K., and Bito, H. (2013). Functional labeling of neurons and their projections using the synthetic activity-dependent promoter E-SARE. Nat. Methods 10, 889–895.

Kim, S.Y., Adhikari, A., Lee, S.Y., Marshel, J.H., Kim, C.K., Mallory, C.S., Lo, M., Pak, S., Mattis, J., Lim, B.K., et al. (2013). Diverging neural pathways assemble a behavioural state from separable features in anxiety. Nature 496, 219–223.

Lammel, S., Ion, D.I., Roeper, J., and Malenka, R.C. (2011). Projection-specific modulation of dopamine neuron synapses by aversive and rewarding stimuli. Neuron 70, 855–862.

**Cell**

Lammel, S., Lim, B.K., Ran, C., Huang, K.W., Betley, M.J., Tye, K.M., Deisseroth, K., and Malenka, R.C. (2012). Input-specific control of reward and aversion in the ventral tegmental area. Nature 491, 212–217.

Lee, A.T., Gee, S.M., Vogt, D., Patel, T., Rubenstein, J.L., and Sohal, V.S. (2014). Pyramidal neurons in prefrontal cortex receive subtype-specific forms of excitation and inhibition. Neuron 81, 61–68.

Lerner, T.N., Shilyansky, C., Davidson, T.J., Evans, K.E., Beier, K.T., Zalocusky, K.A., Crow, A.K., Malenka, R.C., Luo, L., Tomer, R., and Deisseroth, K. (2015). Intact-brain analyses reveal distinct information carried by SNc dopamine subcircuits. Cell 162, 635–647.

Li, X., Zhao, X., Fang, Y., Jiang, X., Duong, T., Fan, C., Huang, C.C., and Kain, S.R. (1998). Generation of destabilized green fluorescent protein as a transcription reporter. J. Biol. Chem. 273, 34970–34975.

Li, B., Piriz, J., Mirrione, M., Chung, C., Proulx, C.D., Schulz, D., Henn, F., and Malinow, R. (2011). Synaptic potentiation onto habenula neurons in the learned helplessness model of depression. Nature 470, 535–539.

Li, K., Zhou, T., Liao, L., Yang, Z., Wong, C., Henn, F., Malinow, R., Yates, J.R., 3rd, and Hu, H. (2013). βCaMKII in lateral habenula mediates core symptoms of depression. Science 341, 1016–1020.

Lin, Y., Bloodgood, B.L., Hauser, J.L., Lapan, A.D., Koon, A.C., Kim, T.K., Hu, L.S., Malik, A.N., and Greenberg, M.E. (2008). Activity-dependent regulation of inhibitory synapse development by Npas4. Nature 455, 1198–1204.

Liu, X., Ramirez, S., Pang, P.T., Puryear, C.B., Govindarajan, A., Deisseroth, K., and Tonegawa, S. (2012). Optogenetic stimulation of a hippocampal engram activates fear memory recall. Nature 484, 381–385.

Long, J.Z., Svensson, K.J., Tsai, L., Zeng, X., Roh, H.C., Kong, X., Rao, R.R., Lou, J., Lokurkar, I., Baur, W., et al. (2014). A smooth muscle-like origin for beige adipocytes. Cell Metab. 19, 810–820.

Matsuda, T., and Cepko, C.L. (2007). Controlled expression of transgenes introduced by in vivo electroporation. Proc. Natl. Acad. Sci. USA 104, 1027–1032.

Matsumoto, M., Matsumoto, K., Abe, H., and Tanaka, K. (2007). Medial prefrontal cell activity signaling prediction errors of action values. Nat. Neurosci. 10, 647–656.

Maya-Vetencourt, J.F., Tiraboschi, E., Greco, D., Restani, L., Cerri, C., Auvinen, P., Maffei, L., and Castrén, E. (2012). Experience-dependent expression of NPAS4 regulates plasticity in adult visual cortex. J. Physiol. 590, 4777–4787.

Menegas, W., Bergan, J.F., Ogawa, S.K., Isogai, Y., Umadevi Venkataraju, K., Osten, P., Uchida, N., and Watabe-Uchida, M. (2015). Dopamine neurons projecting to the posterior striatum form an anatomically distinct subclass. eLife 4, e10032.

Miller, E.K. (2000). The prefrontal cortex and cognitive control. Nat. Rev. Neurosci. 1, 59–65.

Namburi, P., Beyeler, A., Yorozu, S., Calhoon, G.G., Halbert, S.A., Wichmann, R., Holden, S.S., Mertens, K.L., Anahtar, M., Felix-Ortiz, A.C., et al. (2015). A circuit mechanism for differentiating positive and negative associations. Nature 520, 675–678.

Oh, S.W., Harris, J.A., Ng, L., Winslow, B., Cain, N., Mihalas, S., Wang, Q., Lau, C., Kuan, L., Henry, A.M., et al. (2014). A mesoscale connectome of the mouse brain. Nature 508, 207–214.

Pi, H.J., Hangya, B., Kvitsiani, D., Sanders, J.I., Huang, Z.J., and Kepecs, A. (2013). Cortical interneurons that specialize in disinhibitory control. Nature 503, 521–524.

Pinto, L., and Dan, Y. (2015). Cell-type-specific activity in prefrontal cortex during goal-directed behavior. Neuron 87, 437–450.

Sanz, E., Yang, L., Su, T., Morris, D.R., McKnight, G.S., and Amieux, P.S. (2009). Cell-type-specific isolation of ribosome-associated mRNA from complex tissues. Proc. Natl. Acad. Sci. USA 106, 13939–13944.

Schilling, K., Luk, D., Morgan, J.I., and Curran, T. (1991). Regulation of a fos-lacZ fusion gene: a paradigm for quantitative analysis of stimulus-transcription coupling. Proc. Natl. Acad. Sci. USA 88, 5665–5669.

Shah, A.A., and Treit, D. (2003). Excitotoxic lesions of the medial prefrontal cortex attenuate fear responses in the elevated-plus maze, social interaction and shock probe burying tests. Brain Res. 969, 183–194.

Shah, A.A., Sjovold, T., and Treit, D. (2004). Inactivation of the medial prefrontal cortex with the GABAA receptor agonist muscimol increases open-arm activity in the elevated plus-maze and attenuates shock-probe burying in rats. Brain Res. 1028, 112–115.

Shamloo, M., Soriano, L., von Schack, D., Rickhag, M., Chin, D.J., Gonzalez-Zulueta, M., Gido, G., Urfer, R., Wieloch, T., and Nikolich, K. (2006). Npas4, a novel helix-loop-helix PAS domain protein, is regulated in response to cerebral ischemia. Eur. J. Neurosci. 24, 2705–2720.

Shepherd, G.M. (1988). Neurobiology, Second Edition (Oxford University Press).

Smeyne, R.J., Schilling, K., Robertson, L., Luk, D., Oberdick, J., Curran, T., and Morgan, J.I. (1992). fos-lacZ transgenic mice: mapping sites of gene induction in the central nervous system. Neuron 8, 13–23.

Soloway, A.S., Pucak, M.L., Melchitzky, D.S., and Lewis, D.A. (2002). Dendritic morphology of callosal and ipsilateral projection neurons in monkey prefrontal cortex. Neuroscience 109, 461–471.

Spiegel, I., Mardinly, A.R., Gabel, H.W., Bazinet, J.E., Couch, C.H., Tzeng, C.P., Harmin, D.A., and Greenberg, M.E. (2014). Npas4 regulates excitatory-inhibitory balance within neural circuits through cell-type-specific gene programs. Cell 157, 1216–1229.

Tomer, R., Ye, L., Hsueh, B., and Deisseroth, K. (2014). Advanced CLARITY for rapid and high-resolution imaging of intact tissues. Nat. Protoc. 9, 1682–1697.

Tzschentke, T.M., and Schmidt, W.J. (1998). Discrete quinolinic acid lesions of the rat prelimbic medial prefrontal cortex affect cocaine- and MK-801-, but not morphine- and amphetamine-induced reward and psychomotor activation as measured with the place preference conditioning paradigm. Behav. Brain Res. 97, 115–127.

Tzschentke, T.M., and Schmidt, W.J. (1999). Functional heterogeneity of the rat medial prefrontal cortex: effects of discrete subarea-specific lesions on drug-induced conditioned place preference and behavioural sensitization. Eur. J. Neurosci. 11, 4099–4109.

Warden, M.R., Selimbeyoglu, A., Mirzabekov, J.J., Lo, M., Thompson, K.R., Kim, S.Y., Adhikari, A., Tye, K.M., Frank, L.M., and Deisseroth, K. (2012). A prefrontal cortex-brainstem neuronal projection that controls response to behavioural challenge. Nature 492, 428–432.

Xiu, J., Zhang, Q., Zhou, T., Zhou, T.T., Chen, Y., and Hu, H. (2014). Visualizing an emotional valence map in the limbic forebrain by TAI-FISH. Nat. Neurosci. 17, 1552–1559.
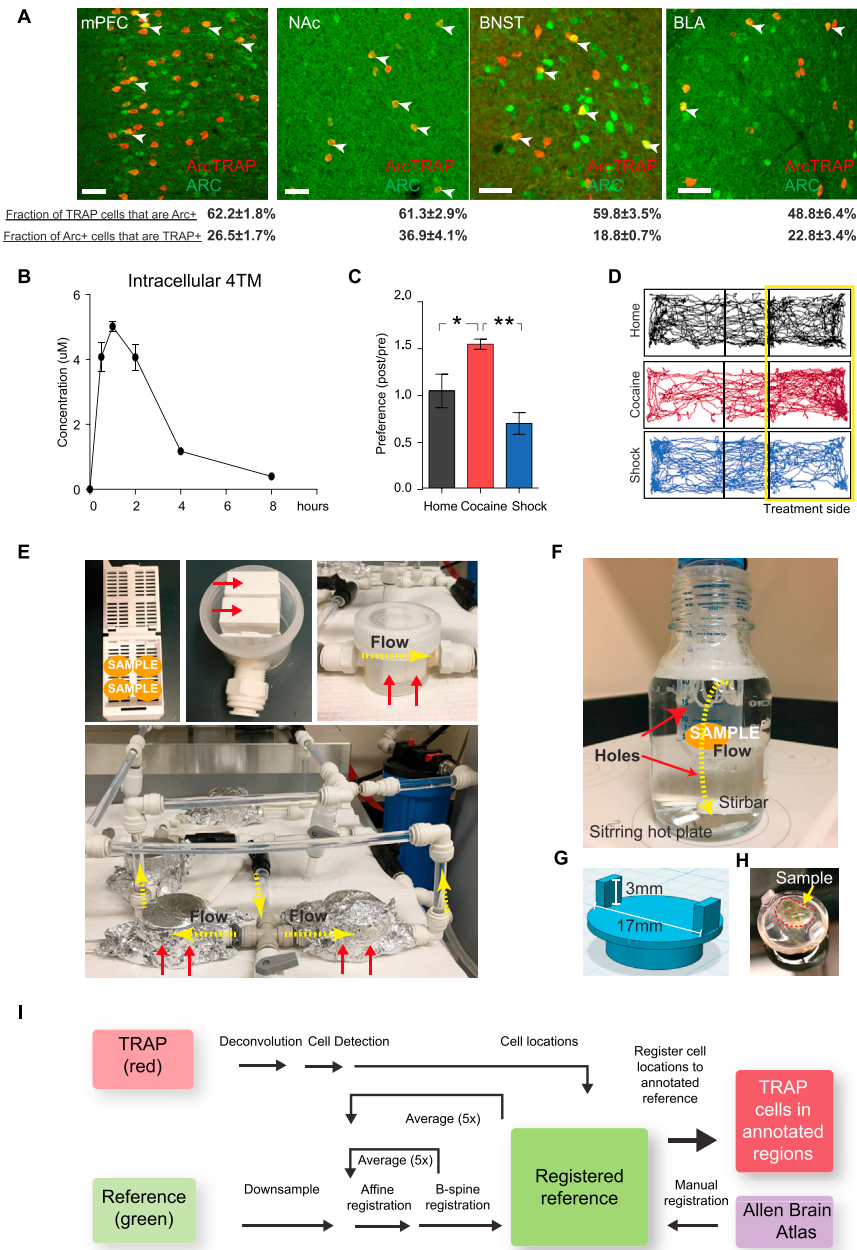
**Figure S1. Behavioral Cohort-Scale Brain-wide Activity Mapping by CLARITY, Related to Figure 1**

(A) Representative images and quantification (mean ± SEM, n = 4 mice per group) of colabeling between ArcTRAP and Arc immunostaining in indicated regions. Arrowheads indicate double-positive cells. Numbers in top row: fraction of ArcTRAPed cells that are Arc+; Bottom row: fraction of Arc+ cells that are ArcTRAPed. Note that the labeling by ArcTRAP is more stringent than Arc immunostaining (fewer TRAP+ cells than Arc+ cells overall). Scale bar: 50 μm.

(B) Pharmacokinetics of 4TM in mouse brain after a single intraperitoneal injection (10mg/kg); n = 5 per time point.

(C) Cocaine dosing (15mg/kg) and a series of foot shocks (0.5mA/2 s) lead to place preference and aversion, respectively. An independent cohort of mice was used to validate the stimuli used in the study as appetitive (cocaine) and aversive (shock) using a 3-chamber place preference test. After two days of indicated exposure, fold-change in preference for the side where cocaine or shock was given was quantified. n = 5 per group, *p < 0.05, **p < 0.01, unpaired t test. Error bars, mean ± SEM.

(D) Representative movement tracking data.

(E) Setup of parallel flow-assisted clearing. Up to 4 mouse brains can be inserted into a tissue cassette (30x40x12mm). Two cassettes (indicated by red arrows) are inserted into a chamber constructed with an inlet and outlet for buffer exchange. To scale up clearing, multiple chambers (each containing up to 8 brains) can be connected in parallel to a temperature-controlled circulator (calibrated so that the temperature in the sample chamber is kept at 40°C).

(F) Alternative flow-assisted clearing setup without using a circulator. A 50ml conical tube (with small holes drilled in the middle and on the bottom, as indicated by red arrows) can be inserted into a 250ml glass bottle filled with clearing buffer. Each tube fits 3-4 mouse brains. Unidirectional flow (yellow line) is created by using

a magnetic stir bar and a stirring hot plate to accelerate the clearing. Upon first use, the temperature of the hot plate needs to be set properly so that the buffer temperature is maintained at desired level inside the conical tube. The speed of the stirring should also be set properly so that proper flow is being generated without damaging the sample.

(G and H) Schematic and picture of the adaptor used for mounting brains onto the ultramicroscope (Lavision Biotec).

(I) Data processing pipeline for image registration, cell detection, annotation and quantification.
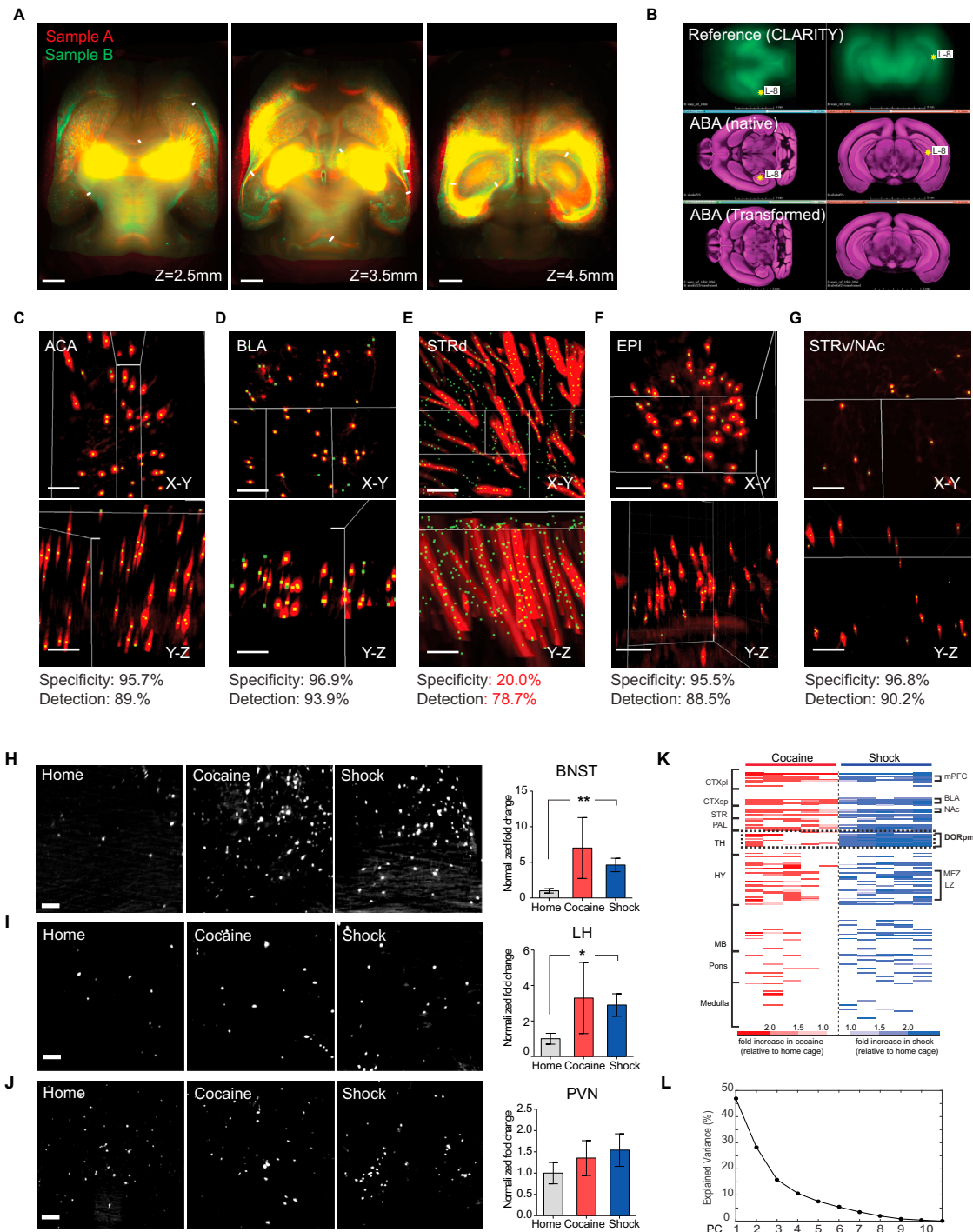
**Figure S2. Cocaine and Shock Recruit Overlapping Brain Regions, Related to Figure 2**

(A) Representative images illustrating alignment between individual brains after registration. TRAP signal from two individuals (one shown as red, the other as green) overlaid to show alignment. White bars indicate small remaining misaligned boundaries due to combined sources of structural variation and alignment error (~200μm). Scale bar: 500 μm.

(B) Representative images illustrating the manual ABA registration using 3D-Slicer. A total of 30 landmarks (showing one (#8) here) were manually placed in the CLARITY reference (top) and the ABA reference (middle). The program calculated the transform (using thin plate registration) and output the transformed ABA image (bottom).

(C–G) Representative images illustrating the automatic 3D cell detection in various brain regions. Top: cell detection in x-y plane; Bottom: cell detection in y-z plane. ACA: anterior cingulate cortex; BLA: basolateral amygdala; STRd: dorsal striatum; EPI: epithalamus; STRv/NAc: ventral striatum/nucleus accumbens.

*(legend continued on next page)*

Note that cell detection failed in STRd as the program could not distinguish fiber bundles from cell bodies. Therefore the STRd was excluded from all subsequent analysis. For quantifying detection accuracy, in each region, the specificity is defined by the percent of cells correctly detected (True positive / (True positive +False positive)) and detection is defined by percent of ground-truth cells detected (True positive/ (True positive + False negative)). Manually identified cells are used as "ground truth." Numbers represent means from three independent counts. Scale bar: 100 $\mu$m.

(H–J) TRAP cells in BNST, LH and PVN. Left: representative images taken at the center of the indicated regions (maximum projection of 100 $\mu$m volume). Scale bar: 100$\mu$m. Right: fold-change in TRAP cell numbers (normalized to home cage). n = 5 per group, *p < 0.05, unpaired t test. Error bars, mean ± SEM.

(K) Heat map showing cocaine- and shock- activated brain regions. Each column represents an individual mouse. Each row represents an individual brain region ($\sim$200 regions in total). Increase in TRAP cell counts in each region was color-coded as fold changes (red: increase cell counts in cocaine group; blue: increase cell counts in shock group; all normalized to home cage controls). Cocaine or shock activated areas were summarized as clusters of proximal regions. CTXpl/sp: cortical plate/subplate, SRT: striatum, PAL: pallidum, TH: thalamus, HY: hypothalamus, MB: midbrain. DORpm: polymodal association cortex-related dorsal thalamus. MEZ: Hypothalamic medial zone, LZ: Hypothalamic lateral zone.

(L) Percentage of total variance explained by each principal component in the PCA (Supplemental Experimental Procedures).
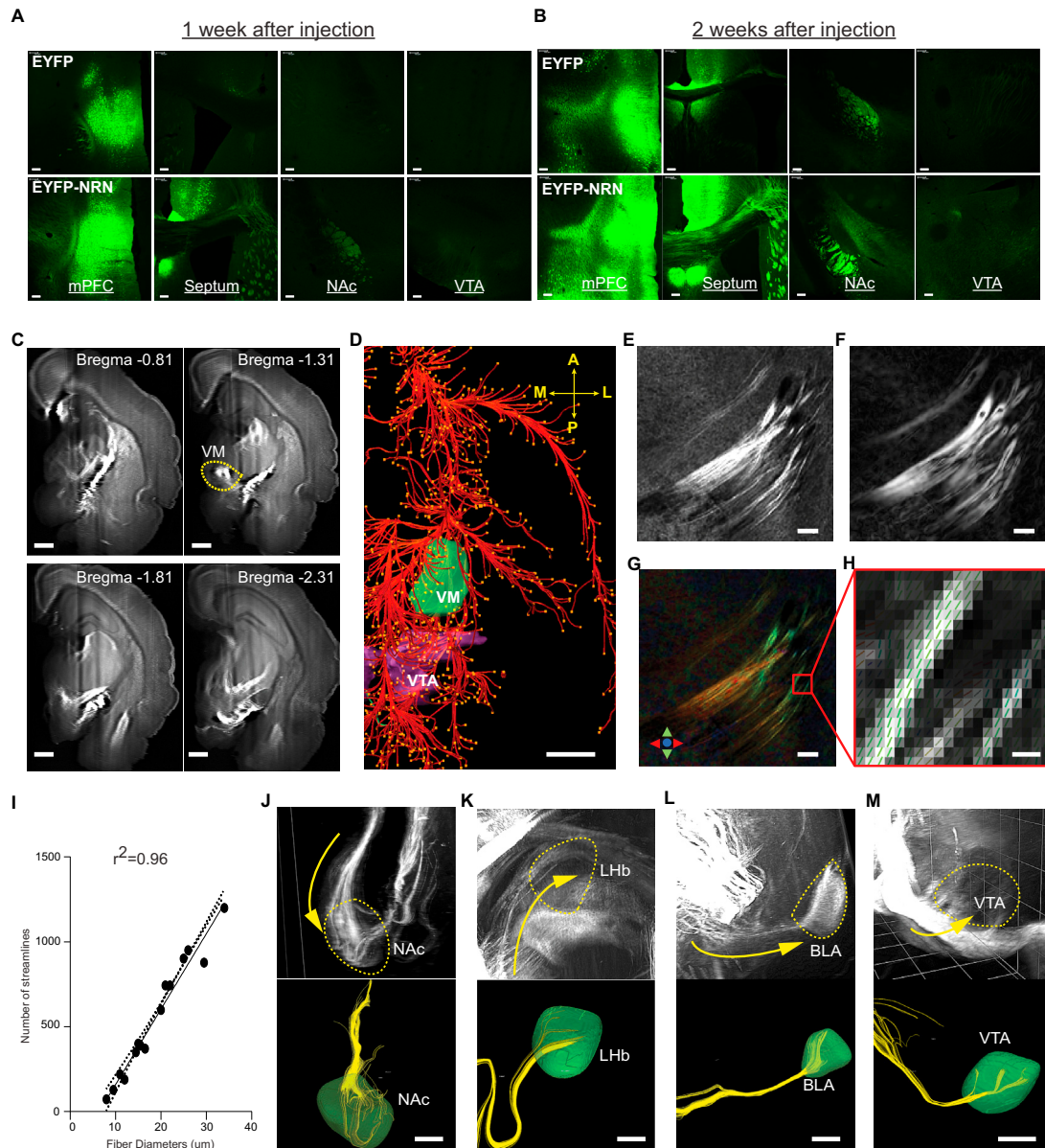
**Figure S3. CLARITY Enables Brain-wide Projection Mapping, Related to Figure 3**

(A and B) Representative images (n = 4 mice per group) showing side-by-side comparisons between EYFP and EYFP-NRN expression in downstream regions after a single mPFC injection (both under a CaMKIIα promoter). Note that EYFP-NRN travels faster than EYFP alone. Scale bar: 100 μm.

(C) 2D coronal sections (50μm max-projection) at the indicated locations (relative to bregma). Scale bar: 500 μm.

(D) A snapshot of putative mPFC to VM (ventral medial thalamus, highlight in green) projection paths (shown as red streamlines) from the Allen Brain mouse connectivity atlas (http://connectivity.brain-map.org/). Scale bar: 1mm.

(E–H) Representative intermediate steps of reconstructing axonal projection to streamlines using structural tensor based CLARITY tractography (Supplemental Experimental Procedures). (E) Raw CLARITY image, showing outgoing mPFC projections (EYFP). (F) Image intensity gradient amplitude, computed by convolving the 3-dimensional CLARITY image volume with three 3-dimensional 1st order derivative of Gaussian functions (σdog = 1 voxel/6 μm) along each of the x, y and z axes. (G) Color-coded principal fiber orientations (A-P: red; D-V, green; L-M, blue), estimated as the tertiary eigenvectors of computed structure tensors (σd = 1 voxel/6 μm, σdog = 1 voxel/6 μm). For better visualization, the color brightness was weighted by the raw CLARITY image intensity. Scale bars: 100 μm. (H) A zoomed-in region of (E) showing the principal fiber orientations as color-coded vector fields overlaid on raw CLARITY image. The vectors are color-coded for their orientation. Scale bar: 6μm.

(I) Correlation between the diameter of each axonal bundle and the number of streamlines representing that specific bundle. The diameter was determined at the cross-sections of each bundle. The numbers of passing streamlines are also measured at the same cross-sections. n = 15, Pearson correlation, $r^2$ = 0.96, p < 0.0001.

(J–M) Representative reconstructions of axonal projections (outgoing projections from mPFC) in various target regions. Top row: CLARITY images; bottom row: reconstructed streamlines ending in the indicated 3D regions.
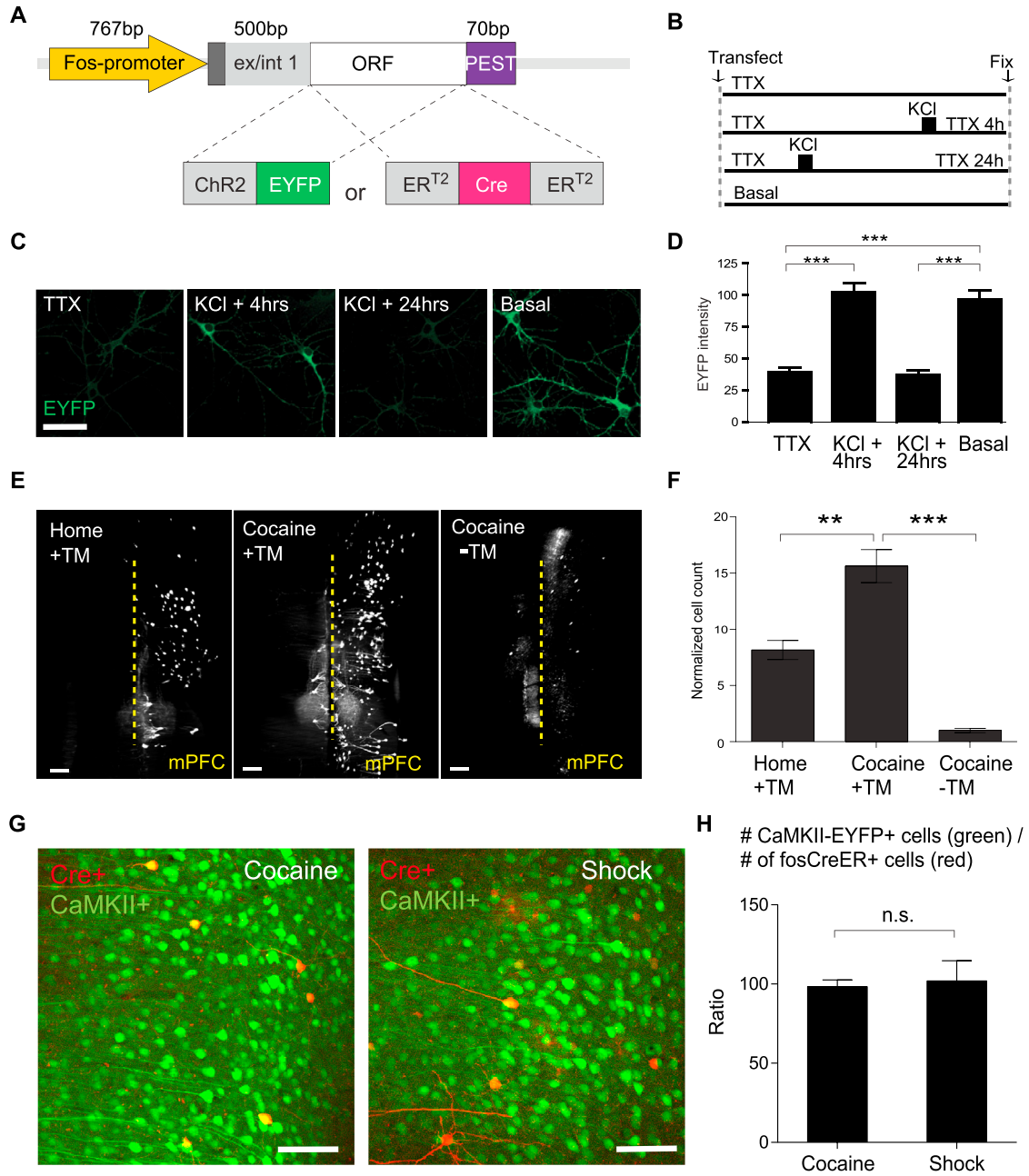
**Figure S4. Validation of Activity-Dependent Constructs, Related to Figure 4**

(A) Construction strategy. An expression cassette was inserted immediately after intron 1 of the c-*fos* gene. Either ChR2-EFYP (cFos-ChR2-EYFP, termed fosCh) or $ER^{T2}$-Cre-$ER^{T2}$ fusion was inserted, followed by a 70bp PEST sequence to promote construct degradation (to further enhance specificity).

(B) Schematic to illustrate treatment of cultured hippocampal neurons following transfection of c-Fos-ChR2-EYFP. Neurons were electrically silenced with TTX, APV and NBQX; fosCh expression was compared to expression levels in "basal" (spontaneously synaptically active, but not otherwise stimulated or silenced) cultures. Following a 30 min depolarizing stimulus (60 mM KCl) the TTX/APV/NBQX solution was replaced and groups were fixed at the indicated time points.

(C) Representative images showing fosCh expression of cultured hippocampal neurons for each of the treatment groups. Scale bar: 25 μm.

(D) Quantification of mean pixel intensity of EYFP expression for conditions represented in c, n = 39-59 cells per group, $F_{3,\ 205}$ = 37.20, \*\*\*p < 0.001, ANOVA followed by Tukey's multiple comparison test. (E-F) AAV-cFos- $ER^{T2}$-Cre-$ER^{T2}$-PEST was injected into the mPFC of Ai14 Cre-reporter mice. The mice were divided into three groups (n = 5 per group): home cage with 4TM, cocaine-injected with 4TM and cocaine-injected without 4TM.

(E) Representative images showing 4TM-dependent and activity-dependent labeling of mPFC neurons (tdTomato+), scale bar: 100 μm.

(F) Quantification tdTomato+ mPFC cells in three groups (normalized to the No-4TM group).

(G and H) Representative images and quantification showing CaMKIIα (green) and fosCreER (red) viruses target neurons at a constant ratio between two conditions. Scale bar: 50 μm. \*\*p < 0.01, \*\*\*p < 0.001, unpaired t test. Error bars, mean ± SEM.
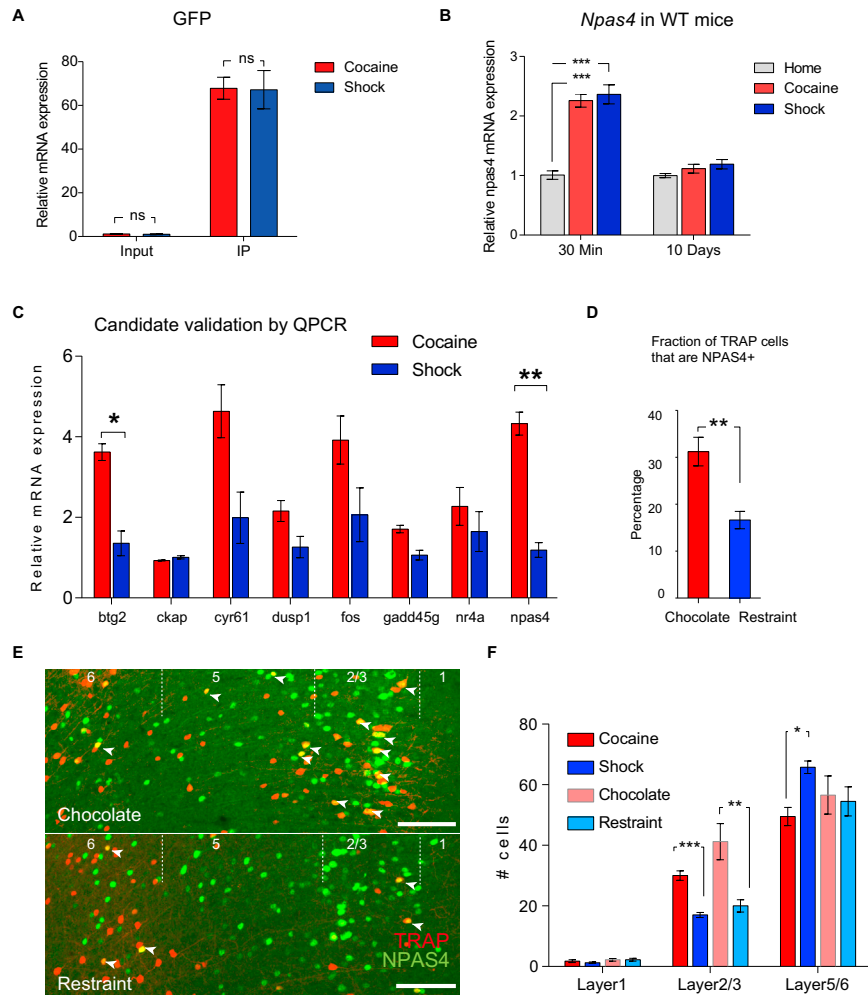
**Figure S5. Positive Valence Experience Preferentially Activates the NPAS4+ Population in mPFC, Related to Figure 5**

(A) Quantitative PCR analysis of GFP mRNA from the input and IP fraction of the cocaine- and shock-tagged mPFC population. Immunoprecipitation lead to 60- to 70-fold enrichment of GFP mRNA under both conditions (comparing Input to IP; Supplemental Experimental Procedures).

(B) Quantitative PCR analysis of mPFC Npas4 mRNA expression in the wild-type mice, 30 min and 10 days after the acute stimuli (cocaine or shock) exposure.

(C) Quantitative PCR validation of candidate genes (showing > 2.0 fold change, disregard p values, from cocaine IP versus shock IP (Figure 5B)). 1 of the 9 genes enriched in cocaine-cells was excluded (Gm6592, predicted gene); 2 of the 2 shock-enriched genes were excluded: ttr (transthyretin, undetectable by QPCR) and zfa (pseudogene). Out of the remaining eight genes, only Npas4 and Btg2 passed qPCR validation (p < 0.05).

(D and E) Quantification and representative images showing the overlap between TRAP+ (labeled by chocolate consumption and restraint; Supplemental Experimental Procedures) and NPAS4+ cells in the mPFC. Arrowheads indicate double positive cells. Scale bar: 100 μm.

(F) Layer distribution of TRAP cells with positive (cocaine or chocolate) experiences and negative (shock or restraint) experiences. n = 4-5 per group, ns, p > 0.05; *p < 0.05; **p < 0.01; ***p < 0.001; unpaired t test with Holm-Sidak correction. Error bars, mean ± SEM.
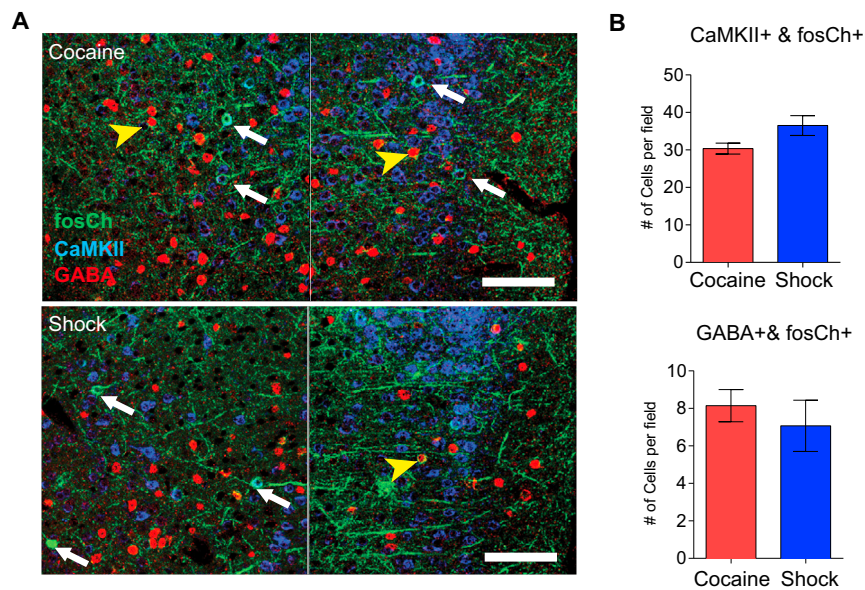
**Figure S6. Use of fosCh for Targeting Cocaine- and Shock-Activated mPFC Populations, Related to Figure 6**

(A) Representative confocal images showing fosCh expression in mPFC sections co-labeled with anti-GABA, and anti-CaMKIIα antibodies as indicated. White arrows indicate fosCh+/CaMKIIα+ neurons. Yellow arrowheads indicate fosCh+/GABAα+ neurons. Two 40X images were stitched together to visualize all cortical lamina. Scale bar = 100 μm.

(B) Quantification revealed no significant difference in the number of CaMKIIα-positive (left) and GABA-positive (right) fosCh cells for cocaine and shock groups. n = 10-14 mice per group. Error bars, mean ± SEM.
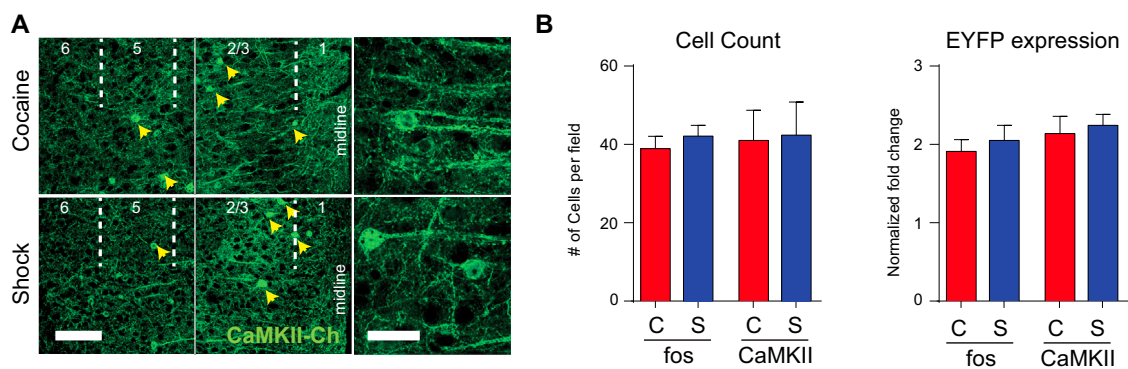
**Figure S7. Use of CaMKIICh for Targeting Non-selective mPFC Populations, Related to Figure 7**

(A) Representative images showing mPFC expression of CaMKIIα-ChR2 control conditions. Left, two 40X images were stitched together to visualize all cortical lamina. Scale bar = 100 μm. Right, high magnification images of individual CaMKIIα-ChR2 neurons. Scale bar = 25 μm.

(B) Quantification revealed no significant difference in the number of labeled cells (left) or level of EFYP expression (right) between CaMKIIα-ChR2 and fosCh conditions. n = 13 mice per group. Error bars, mean ± SEM.

# Supplemental Information

# Wiring and Molecular Features of Prefrontal

# Ensembles Representing Distinct Experiences

Li Ye, William E. Allen, Kimberly R. Thompson, Qiyuan Tian, Brian Hsueh, Charu Ramakrishnan, Ai-Chi Wang, Joshua H. Jennings, Avishek Adhikari, Casey H. Halpern, Ilana B. Witten, Alison L. Barth, Liqun Luo, Jennifer A. McNab, and Karl Deisseroth

## Supplemental Experimental Procedures

## Constructs

The pAAV-fos-ChR2-EYFP (fosCh) plasmid was constructed by fusing the codon-optimized ChR2 (H134R) tagged with enhanced yellow fluorescent protein to a truncated c-fos gene sequence that included the 767 bp minimal promoter segment and the 500 bp intron 1 coding region containing key regulatory elements. A 70 bp PEST sequence was inserted at the C-terminal end to promote degradation and thereby prevent the membrane targeted ChR2-YFP from accumulating over time. The construct was cloned into an AAV backbone. The pAAV-fos-ER$^{T2}$-Cre- ER$^{T2}$-PEST plasmid was constructed by replacing the ChR2-EYFP in the fosCh plasmids with an ER$^{T2}$-Cre-ER$^{T2}$ cassette (Kawashima et al., 2013). The pAAV-CaMKIIα-EYFP-NRN plasmid was constructed by replacing the 479 bp hGH polyA tail in pAAV-CaMKIIα-eYFP-WPRE-hGHpa (Tye et al., 2011) with a DNA fragment containing the 992 bp 3' UTR of Neuritin plus 215 bp bGH poly A flanked by AfeI and BstEI sites (NRN from the 3' UTR of the rat neuritin mRNA, (NM_053346.1)) (Akten et al., 2011).

## Virus and injection

Adeno-associated viral (AAV) vectors were serotyped with AAV5 or AAV8 coat proteins and packaged by the University of North Carolina Vector Core and Stanford University Vector Core. Injections were made unilaterally into the PFC with final viral concentrations of AAV8-fos-ERT2-Cre-ERT2-PEST: $3x10^{12}$, AAV8-CaMKIIα-EYFP-NRN: $1.5x10^{12}$, AAV8-EF1α-DIO-EYFP-NRN: $5x10^{12}$, AAV5-fosCh-YFP: $2x10^{12}$, AAV5-CaMKIIα-YFP: $1.5x10^{11}$, all as genome copies per mL.

## Stereotaxic surgery

6-7-week-old mice were anaesthetized with 1.5–3.0% isoflurane and placed in a stereotaxic apparatus (Kopf Instruments). Surgeries were performed under aseptic conditions. A scalpel was used to open an incision along the midline to expose the skull. After performing a craniotomy, viruses was injected into the mPFC using a 10 μl nanofil syringe (World Precision Instruments) at 0.1 μl min−1. The syringe was coupled to a 33 gauge beveled needle, and the bevel was placed to face the anterior side of the animal. The syringe was slowly retracted 20 min after the start of the infusion. A slow infusion rate followed by 10 min of waiting before retracting the syringe was crucial to restrict viral expression to the target area. Infusion coordinates were: anteroposterior, 1.9 mm; mediolateral, 0.35 mm; dorsoventral, 2.6 mm. Coordinates for the unilateral implantation of fiber optic cannulae (Doric Lenses 200 μm diameter) were: anteroposterior, 1.9 mm; mediolateral, 0.35 mm; dorsoventral, -2.4 mm. All coordinates relative to bregma.

## ArcTRAP labeling

Male ArcTRAP (ArcCreER+/-, Ai14+/-) mice were used for study. 6-7 week old ArcTRAP mice were handled and injected with saline daily for at least 5 days prior to the experiment (including the home cage controls) to minimize the labeling due to handling and injections. The mice were 7-8 weeks old at the time of behavioral labeling. On experimental day 0, animals from both cocaine and shock groups were individually placed in a plastic chamber equipped with a grid floor connected to a shock generator, for 10 minutes to acclimatize the animals to the chamber (without receiving any actual shock or cocaine). On the following two days (experimental day 1 and day 2), animals were individually placed in the chamber for 10 minutes right after receiving 15 mg/kg intraperitoneal cocaine (cocaine group) or to receive 20 random foot shocks (2s, 0.5mA, 2 shocks per minute on average, shock group). The home cage control group remained in their home cage for the whole period. All the chambers were cleaned with 70% ethanol between trials. On experimental day 2, all mice received 5 mg/kg 4TM (IP injection) 3 hours after the behavioral challenge to enable TRAP labeling.

For ArcTRAP and Arc dual labeling: the mice were shocked (using the protocol above) in the presence of 5 mg/kg 4TM. The same animals were shocked again 96 hours after the first shock session and sacrificed 60 minutes later for Arc immunostaining. To verify that the resulting high level of overlap (~60%) in cells activated by different presentations of the same experience was not attributable to a population of constitutively active neurons in a particular field of view with activity unrelated to stimulus presentation, a shock-TRAPped animal was acutely injected with cocaine to label contrasting experiences (TRAP: shock; Arc staining: cocaine), which was found to result in low TRAP/Arc overlap in the mPFC (29.4±1.4%, as fraction of TRAP cells that were Arc+, or 14.0±2.4% as fraction of Arc+ cells that were TRAP+; mean± s.d., n=3 technical repeats from multiple fields of view). This finding was quantitatively replicated in a second animal (resulting 32.8±2.4% of TRAP cells that were Arc+ or

13.3±2.6% Arc+ cells that were TRAP+). These findings are also concordant with and supported by earlier work in the same mouse line (in the original TRAP paper; Guenthner et al, Neuron, 2013).

For labeling with a different set of positive/negative experiences: mice were individually housed one week before the experiments. On experimental day 1, a food pellet (1 gram mixture of milk chocolate and peanut butter) was given to the chocolate group for 1 hour to familiarize them with chocolate. The other group were restrained in rodent restrainer for 1 hour. On day 2, same chocolate pellets were given to the chocolate group and at least 0.5g was consumed within 1 hour. The restrain group were restrained again for 1 hour. Both groups received 5 mg/kg 4TM 3 hours after the beginning of the treatments to label the activated cells. All groups, including the home cage controls, received 4-hyroxytamoxifen injections at the same time of the day (2-3PM). The bedding of all cages was refreshed daily for 48 hours to prevent 4TM retake. All labeled mice were kept in their home cage for an additional 10 days to allow the full expression of tdTomato before perfusion.

### Activity-dependent ribosome labeling

Male Arc-rTag mice were trained and labeled with 4TM with the same protocol used in ArcTRAP labeling. After labeling, the mice were returned and kept in their home cage for 14 days to allow full integration of tagged ribosomes.

### Delivery of 4-hydroxytamoxifen

An aqueous formulation (instead of oil, which tends to give slower drug release) is designed to facilitate transient 4TM delivery (Ye et al., 2012). 10mg of 4TM (Sigma H6278) was first dissolved in 250 μl DMSO. This stock is first diluted in 5 ml of saline containing 2% Tween 80 and then diluted 1:1 again with saline. The final injectable solution contained: 1 mg/ml 4TM, 1% Tween 80 and 2.5% DMSO in saline. The pharmacokinetics of 4TM in mouse brain (using the above vehicle) was determined using a standard LS-MS method at Biomaterials and Advanced Drug Delivery Laboratory at Stanford. Briefly, 30 C57BL/6J mice were injected (IP) with 10 mg/kg 4TM at indicated time points (n=5 each time point) and n=5 mice injected with vehicle alone were used as blank control. Brains were collected after perfusion using 1X PBS at different time points and snap-frozen in liquid nitrogen before homogenized for Liquid Chromatography Mass Spectrometry (LC-MS) analysis.

### CLARITY processing

The three key features of this new approach were: 1) accelerated clarification through parallelized flow-assisted clearing crucial for large cohorts (Figure S1D-G) independent of specialized equipment such as electrophoresis or perfusion chambers; 2) >90% cost reduction (also important for these large behavioral cohorts) using a new refractive index-matching process; and 3) optical properties such that the whole mouse brain can be imaged using a commercial light-sheet microscope under a single field of view (FOV) and as a single stack (~1200 steps across a ~6.6mm range) in less than 2 hours with single-cell resolution throughout the whole volume (this speed and simplicity is also critical for large behavioral cohorts; Figure 1C, D). Raw data files from each brain are ~12 GB in size and can be easily stored and directly analyzed on standard desktop workstations without the need for compression or stitching.

A hydrogel based on 1% acrylamide (1% acrylamide, 0.125% Bis, 4% PFA, 0.025% VA-044 initiator (w/v), in 1X PBS) was used for all CLARITY preparations. Mice were transcardially perfused with ice-cold 4% PFA. After perfusion, brains were post-fixed in 4% PFA overnight at 4°C and then transferred to 1% hydrogel for 48 hours to allow monomer diffusion. The samples were degassed and polymerized (4-5 hours at 37°C) in a 50ml tube. The brains were removed from hydrogel and washed with 200mM NaOH-Boric buffer (pH=8.5) containing 8% SDS for 6-12 hours to remove residual PFA and monomers. Brains could now be transferred to a flow-assisted clearing device using a temperature-control circulator or a simpler combination of 50ml tube and heated stirring plate (Figure S1D-E). 100mM Tris-Boric Buffer (pH=8.5) containing 8% SDS was used to accelerate the clearing (at 40°C). Note that Tris-containing buffer should only be used after PFA is completely washed out as Tris may potentially interact with PFA. With this setup, a whole mouse brain can be cleared in 12 days (with circulator, or 8 days for a hemisphere) or 16 days (with conical tube/stir bar). After clearing, the brain was washed in PBST (0.2% Triton-X100) for at least 24 hours at 37°C to remove residual SDS. Brains were incubated in a refractive index matching solution (RapidClear, RI=1.45, Sunjin lab, http://www.sunjinlab.com/) for 8 hours (up to 1 day) at 37°C and then 6-8 hours at room temperature. After the RC incubation, the brains were ready for imaging.

A 2-step TSA amplification strategy was used for immunostaining in thick CLARITY sections (such as the NPAS4 staining in Movie S1) to ensure homogeneous staining throughout the depth. 2mm sections were first stained with anti-NPAS4 antibody (1:3000, 6 days at 4°C in 0.3% PBST) and then stained with a secondary antibody conjugated with HRP (1:1000, 4 days at room temperature in 0.3% PBST). Samples were washed at least 24 hours at room temperature between steps. After $2^{nd}$ antibody, samples were first incubated with TSA-Cy5 substrate (1:50, Perkin Elmer) or Alexa 647 Tyramide (1:50, Molecular Probes) in PBST containing 20% DMSO and 0.3% Triton-X100 (instead of the TSA amplification buffer or $H_2O_2$) at room temperature for 4 hours to allow efficient penetration of the substrate without reacting with HRP. Samples were then switched to TSA amplification buffer or 0.0015% $H_2O_2$ containing TSA-Cy5 substrate or Alexa 647 Tyramide (1:200) for additional 20 minute at room temperature to allow tyramide labeling. Samples were thoroughly washed for another 24 hours in 0.3% PBST at room temperature before mounting and imaging.

## CLARITY imaging

*Light-sheet imaging:* Whole brain and hemisphere images were acquired with the Ultramicroscope II (Lavision Biotec). Samples were mounted to a custom 3D printed holder (Figure S1F-G) using RapidClear Mounting Gel (Sunjin lab). For whole brains (TRAP brains), the brain was mounted with the ventral side on top. For hemisphere, the cut surface (midline of the brain) was placed in touch with the holder and with the most lateral part on the top. Samples were securely mounted to the holder after mounting gel solidified (~5 minute at 4°C). Mounted samples were imaged inside an imaging chamber filled with 150ml of Rapidclear (reusable by periodical filtering). Samples were left in imaging chamber for 20-40min before imaging to allow the equilibrium of imaging liquid. Brains were imaged using a 2x/0.5NA objective at 0.6x zoom (whole brain, TRAP) or 0.8x zoom (hemisphere, CAPTURE). Multi-color imaging was enabled by applying filters setting to a supercontinuum white laser (NKT photonics). Samples were with two light sheets (NA=0.144) illuminating from both sides of the sample. Z-step was set to 5.16µm (at 0.6x zoom) or 4µm (at 0.8x zoom). Five horizontal focal points were set to each imaging plane for creating a homogeneous field of view.

*Confocal imaging (Movie S1):* Clarified tissues (2mm coronal sections) were incubated in Rapidclear CS for 1 day and mounted using a Wilco dish. The tissues were then imaged using an Olympus FV1200 system equipped with a 10x water-immersion objective (numerical aperture: 0.6; working distance: 3mm; step size, 3µm).

## Image processing and visualization

All raw images were acquired as 16-bit TIFF files. The raw images were further processed by blind 3D deconvolution using AutoQuantX3 (Media Cybernetics). The parameters of the deconvolution were based on published methods using a similar light sheet microscope with a few modifications (Tainaka et al., 2014). Briefly, the modality was set to "Multi-photon fluorescence" 3D-blind deconvolution with 20 iterations. Noise was set to zero and using "unfiltered image" as "initial guess". In the expert settings, montage was turned on XY but off on Z, with 30-pixel overlap in XYZ. Other settings such as NA, spacing and magnitude were set based on the actual experiments. Either deconvolved or raw images can be 3D-rendered and visualized using Imaris (Bitplane, v8.1.2), for taking snapshot images and making movies.

## Registration and quantification (TRAP analysis)

Briefly, after deconvolution, images of the TRAP brains were downsampled 4x, a subset were used to generate an average reference brain, individual samples were nonlinearly registered to that average reference, and then that registration was applied to the locations of individual cells to count cell numbers using an anatomical atlas in the reference space. Registration was performed on the reference (autofluorescence channel) using elastix(Klein et al., 2010).

Detailed procedures: To initialize the reference, 21 brains and their reflection across the midline axis of the image volume (total of 2*21=42 samples) were globally aligned to the Allen Brain Atlas Nissl-stained volume and then averaged. Each brain was then affine registered to the current average five times, and then resulting registered brains were again averaged to provide the input to the next iteration. Finally, all the brains were nonlinearly registered to the current reference (using an affine transformation as initialization), then averaged, for five iterations.

Each of the experimental samples was then nonlinearly registered to the average reference. Cell locations were detected in deconvolved images using Imaris (v8.1.2 Bitplane). The resulting nonlinear transformation for each brain was applied to every cell location found. Binary mask volumes were made for each brain region in the atlas

either manually drawn or from aligned Allen Brain Atlas (manually registered using 30 landmarks, using 3D-slicer http://www.slicer.org/ ) and indices from these mask volumes were used to compute the number of warped cell locations in each anatomical region. Of note, we excluded the regions where ArcTRAP is known to have strong non-tamoxifen dependent labeling (hippocampus, somatosensory and motor cortex)(Guenthner et al., 2013). Also, consistent with the original paper, AcrTRAP labeling was mainly in the forebrain; therefore, although we detected sparse signal/changes in the broader midbrain/hindbrain regions, the manual validation and analysis was focused on the forebrain. Principal component analysis was performed in MATLAB on the fold-change values relative to controls of all brain regions containing non-zero values.

Manually-defined brain regions: the 3D reference brain was digitally resliced into coronal sections with 100 μm spacing. Eight regions were drawn onto every coronal section with manually identified boundaries based on Allen Brain Atlas. The 2D contours were then used to generate a 3D surface using Imaris to quantify the cell numbers for each brain region.

### Histology

Mice were deeply anaesthetized and transcardially perfused with ice-cold 4% paraformaldehyde (PFA) in PBS (pH 7.4). Brains were fixed overnight in 4% PFA and then equilibrated in 30% sucrose in PBS. 40 μm thick coronal sections were cut on a freezing microtome and stored in cryoprotectant at 4°C until processed for immunostaining. Free-floating sections were washed in PBS and then incubated for 30 min in 0.3% Triton X-100 (Tx100) and 3% normal donkey serum (NDS). Slices were incubated overnight with 3% NDS and primary antibodies including: rabbit anti-GABA (Sigma A2052 1:200), mouse anti-CaMKIIα (Abcam ab22609 1:200), chicken anti-GFP (Abcam ab13970 1:500), Arc (SYSY 156003, 1: 4000) and rabbit anti-NPAS4 (a gift from Michael Greenberg, 1:3000). Sections were then washed and incubated with secondary antibodies (Jackson Labs 1:1000) conjugated to donkey anti-rabbit Cy5, anti-mouse Cy3 and anti-chicken FITC for 3 hrs at room temperature. All Arc and NPAS4 staining was performed using a TSA-plus-Cy5 amplification system (Perkin Elmer). Following a 20 min incubation with DAPI (1:50,000) sections were washed and mounted on microscope slides with PVA-DABCO. Confocal fluorescence images were acquired on a Leica TCS SP5 scanning laser microscope using a 40X/1.25NA oil immersion objective or a 10X/0.6NA water immersion objective. Serial stack images covering a depth of 20 μm (for fosCh experiments) or 40 μm (all other experiments) through multiple sections were analyzed by an experimenter blind to treatment condition. A 700 x 350 μm region of interest (ROI) centered in dorsal mPFC (manually defined based on DAPI staining) was used for cell counting. Average cell counts from five coronal slices (per mouse) were used as "# of cells per field" in all quantifications.

### Ribosome profiling and molecular biology

Immunoaffinity purification of ribosome RNA from mPFC was carried out similarly to a protocol previously described(Sanz et al., 2009) with minor modifications. For preparation of anti-GFP-conjugated dynabeads, for each sample 50 μl protein G dynabeads (Life Technologies) was first washed with PBST and then incubated with 2 μl anti-GFP antibody (Abcam, ab290) in a total volume of 200 μl PBST. After incubating for at least 20 min at room temperature, the PBS-T was removed and the tissue lysates were immediately added to the beads, as described below. mPFC tissue was harvested using a 2mm-diameter tissue punch on freshly cut 2mm-thick coronal sections (cut using pre-chilled brain matrix). mPFC from 5 brains were pooled into one tube and then manually dounce-homogenized in 1 ml of IP buffer [50 mM Tris, pH 7.5; 12 mM MgCl2; 1%NP-40; 100 μg/ml cycloheximide (Sigma); 0.5 mM DTT; 100 mM KCl; 1x HALT protease inhibitor EDTA-free (Thermo); 1 mg/ml sodium heparin (Sigma); 0.2 units/μl RNasin (Promega)]. Following vortexing and centrifugation (12,000 x g for 10 min), 50 μl of the supernatant was taken as "input", and the remaining supernatant was incubated with the anti-GFP conjugated dynabeads for immunoprecipitation (IP fraction). After 2 h at 4°C, dynabeads were separated and washed twice with 1 ml high salt buffer [50 mM Tris, pH 7.5; 12 mM MgCl2; 1% NP-40; 100 μg/ml cycloheximide (Sigma); 0.5 mM DTT; 300 mM KCl]. Following the last wash, TRIzol (500 μl, Life Technologies) was immediately added to the beads (IP fraction). Another 500 μl TRIzol was added to the 50 μl input fraction collected earlier. RNA was purified using RNeasy Micro Kit (Qiagen) according to the manufacturer's instructions. RNA samples (all at 100ng per sample) were processed at the Stanford Protein and Nucleic Acid Biotechnology Facility by one-cycle target preparation, labeling and hybridization to Mouse Gene 2.0 ST Array (Affymetrix), according to the manufacturer's protocol and analyzed by Affymetrix Transcriptiome Analysis Console. The accession number for the microarray data reported in this paper is GEO: GSE76851. For qPCR analysis, RNA was reverse transcribed using the ABI high

capacity cDNA synthesis kit and used in quantitative PCR reactions containing SYBR-green fluorescent dye (ABI). Relative expression of mRNAs was determined after normalization with TBP levels using the $\Delta\Delta$Ct method.

## Reconstruction and analysis of projections

Tractography methodology akin to what is used for diffusion MRI was used to reconstruct 3D models of fiber bundle trajectories based on the CLARITY data. The tractography algorithm (Mori et al., 1999) propagates streamlines from a "seed" region through a vector field of voxel-wise principal fiber orientations and terminates if a streamline makes a sharp turn (angles larger than a prescribed threshold $\alpha_{thresh}$) or ventures outside of the masked region. The "seed" region (injection site) is manually identified based on the actual boundaries of maximal CaMKII$\alpha$-EYFP expression (green signal), which for the experiments presented in Fig. 4 were measured to span: anteroposterior, 2.0±0.06 to 1.5±0.05 mm; mediolateral, 0 to 0.5±0.06 mm; dorsoventral, 2.0±0.07 to 2.9±0.08 mm (all relative to Bregma) and were indistinguishable between experimental groups (p>0.05, multiple t-tests on every axis, n=6 each group); the experimenter was blind to the treatment groups while marking the injection sites. For each voxel, the principal fiber orientation was estimated from a structure tensor, which was computed using the image intensity gradients (as a marker of the edges of fiber tracts) within a local neighborhood of the voxel (Bigun and Granlund, 1987; Budde and Annese, 2012; Budde and Frank, 2012; Kass and Witkin, 1987; Khan et al., 2015; Wang et al., 2015). The principal fiber orientation was defined as the tertiary eigenvector (i.e. with the smallest eigenvalue) of the structure tensor. The structure tensor was defined as:

$$S_w(\boldsymbol{p}) = \iiint_{\mathbf{R}^3} w(\boldsymbol{r}) S_0(\boldsymbol{p} - \boldsymbol{r}) d\boldsymbol{r} \tag{1}$$

where $\boldsymbol{p}$ and $\boldsymbol{r}$ represent spatial locations, $w$ is a Gaussian weighing function with standard deviation $\sigma_g$, $S_0$ is a symmetric second-moment matrix derived from image intensity gradients:

$$S_0(\boldsymbol{p}) = \begin{pmatrix} (I_x(\boldsymbol{p}))^2 & I_x(\boldsymbol{p})I_y(\boldsymbol{p}) & I_x(\boldsymbol{p})I_z(\boldsymbol{p}) \\ I_y(\boldsymbol{p})I_x(\boldsymbol{p}) & (I_y(\boldsymbol{p}))^2 & I_y(\boldsymbol{p})I_z(\boldsymbol{p}) \\ I_z(\boldsymbol{p})I_x(\boldsymbol{p}) & I_z(\boldsymbol{p})I_y(\boldsymbol{p}) & (I_z(\boldsymbol{p}))^2 \end{pmatrix} \tag{2}$$

where $I_x$, $I_y$ and $I_z$ are the gradients of image intensity $I$ along each of the x, y and z axes, computed by convolving $I$ with three 3-dimensional 1st order derivative of Gaussian functions of standard deviation $\sigma_{dog}$ (Canny, 1986). Structure tensors were computed using MATLAB software (MathWorks, Inc.). Tractography and tractography visualization were performed using Diffusion Toolkit and TrackVis softwares (http://trackvis.org/) respectively.

## Cell culture and *in vitro* activity testing

Primary cultured hippocampal neurons were prepared from P0 Spague-Dawley rat pups and grown on glass coverslips as previously described(Gradinaru et al., 2010). At 12 div cultures were transfected with 1 μg fosCh DNA using calcium phosphate. Immediately following the transfection procedure, cultures were returned to Neurobasal-A culture media (Invitrogen Carlsbad, CA) containing 1.25% FBS (Hyclone, Logan, UT), 4% B-27 supplement (GIBCO, Grand Island, NY), 2 mM Glutamax (GIBCO), and FUDR (2 mg/ml, Sigma, St. Louis, MO) to maintain high basal levels of intrinsic synaptic activity, or they were incubated in unsupplemented Neurobasal media that contained 1 μM tetrodotoxin (TTX), 25 μM 2-amino-5-phosphonopentanoic acid (APV) and 10 μM 2,3-dihydroxy-6-nitro-7-sulfamoyl-benzo[f]quinoxaline-2,3-dione (NBQX) to silence electrical activity. Cultures were stimulated for 30 min by exchanging the media with 60 mM isotonic KCl solution and then fixed with 4% PFA at indicated time points.

## *In vivo* optrode recording

Simultaneous optical stimulation and extracellular electrical recording were performed in isofluorane-anesthetized mice. Optrodes consisted of a tungsten electrode (1 MΩ; 125 μm outer diameter) glued to an optical fiber (300 μm core diameter, 0.37 N.A.), with the tip of the electrode projecting beyond the fiber by 300-500 mm. The optical fiber was coupled to a 473 nm laser and 5 mW light measured at the fiber tip was delivered at 10Hz (5 ms pulses). Signals were amplified and band-pass filtered (300Hz low cut- off, 10 kHz high cut-off) before digitizing and recording to disk. pClamp 10 and a Digidata 1322A board were used to both collect data and generate light pulses through the fiber. The recorded signal was band pass filtered at 300Hz low/5 kHz high (1800 Microelectrode AC Amplifier).

Stereotaxic guidance was used for precise placement of the optrode, which was lowered through the dorsal-ventral axis of the mPFC by 50 μm increments. The percentage of sites yielding light-evoked action potential firing was determined.

**Real-time conditioned place preference**

Behavioral experiments were performed 2 weeks after virus injections (1.5 μl) during the animals' dark (active) cycle. For induction of fosCh expression under appetitive or aversive conditions, mice received either i.p. injections of cocaine (15 mg/kg) or underwent 20 random foot shocks (2s, 0.5mA, 2 shocks per minute on average). Mice were exposed to appetitive or aversive training twice a day over 5 consecutive days. Conditioned place preference (CPP) was conducted within 12-16 hours after the last appetitive or aversive training. The CPP apparatus consisted of a rectangular chamber with one side compartment measuring 23 cm x 26 cm with multicolored walls, a central compartment measuring 23 cm x 11 cm with white plexiglass walls, and another side compartment measuring 23 cm x 26 cm with distinctive striped walls. Chamber wallpapers were selected such that mice did not display average baseline bias for a particular chamber, and any mouse with a strong initial preference for a chamber was excluded (more than 5 min difference spent in the side chambers during the baseline test). Automated video tracking software (BiObserve) was used to monitor mouse location over 3 consecutive 20 min blocks to assess place preference behavior before, during and after optogenetic stimulation of the fosCh labeled cells. During the light stimulation block, the laser was automatically triggered upon mouse entry into a pre-designated chamber (fully counterbalanced for side) to deliver 2 sec bursts of 10 Hz light pulses every 5 sec (5 ms pulses at 5 mW) for the duration that the mouse remained in the stimulation side. Data are expressed as fold-change in time spent in the light-paired side relative to the initial baseline preference.

**Statistics**

Two-way ANOVAs were used to assess how gene expression or behavior was affected by other factors (e.g. neuronal activity, optogenetic manipulations). If a statistically significant effect was observed, post hoc testing with correction for multiple comparisons was performed using Tukey's multiple comparisons test. Unpaired t-tests were used for comparisons between two groups. Two-tailed tests were used throughout with $\alpha = 0.05$. Multiple comparisons were adjusted with the false discovery rate method. The experimenter was blinded to the experimental groups while running behavioral experiments and analyzing images. In all figure legends n refers to biological replicates.

**Software**

All custom software, including the scripts used for atlas building, registration, and analysis as well as codes for CLARITY-based tractography are freely available at: http://capture-clarity.org. The website also provides detailed protocols, sample images and other CLARITY-related resource for download.

**Supplemental Table S1, related to Figure 2**

|  |  | PFC | NAC | BNST | LH | LHb | PVN | BLA | CEA |
|---|---|---|---|---|---|---|---|---|---|
| **Home** | **Mean** | 728.8 | 811.8 | 83.6 | 203.6 | 166.8 | 38.4 | 259.2 | 343.6 |
|  | **SEM** | 151.6 | 183.2 | 26.4 | 65.1 | 33.6 | 10.0 | 77.2 | 53.1 |
| **Cocaine** | **Mean** | 1937.2 | 3042.0 | 674.4 | 790.6 | 519.6 | 62.6 | 699.0 | 525.6 |
|  | **SEM** | 269.6 | 871.7 | 388.3 | 437.8 | 226.6 | 12.6 | 123.0 | 85.7 |
| **Shock** | **Mean** | 1334.0 | 3671.0 | 449.6 | 678.0 | 1841.6 | 64.0 | 1068.0 | 731.2 |
|  | **SEM** | 209.8 | 837.1 | 55.6 | 108.0 | 433.3 | 14.1 | 225.8 | 179.6 |

Table S1: Number of TRAP cells in brain regions, before normalization, n=5 in each group.

## Supplemental References

Akten, B., Kye, M.J., Hao le, T., Wertz, M.H., Singh, S., Nie, D., Huang, J., Merianda, T.T., Twiss, J.L., Beattie, C.E.*, et al.* (2011). Interaction of survival of motor neuron (SMN) and HuD proteins with mRNA cpg15 rescues motor neuron axonal deficits. Proc Natl Acad Sci U S A *108*, 10337-10342.

Bigun, J., and Granlund, G.H. (1987). Optimal Orientation Detection of Linear Symmetry. Proceedings of the IEEE First International Conference on Computer Vision, 433-438.

Budde, M.D., and Annese, J. (2012). Quantification of anisotropy and fiber orientation in human brain histological sections. Frontiers in integrative neuroscience *7*, 3.

Budde, M.D., and Frank, J.A. (2012). Examining brain microstructure using structure tensor analysis of histological sections. NeuroImage *63*, 1-10.

Canny, J. (1986). A computational approach to edge detection. Pattern Analysis and Machine Intelligence, IEEE Transactions on, 679-698.

Gradinaru, V., Zhang, F., Ramakrishnan, C., Mattis, J., Prakash, R., Diester, I., Goshen, I., Thompson, K.R., and Deisseroth, K. (2010). Molecular and cellular approaches for diversifying and extending optogenetics. Cell *141*, 154-165.

Guenthner, C.J., Miyamichi, K., Yang, H.H., Heller, H.C., and Luo, L. (2013). Permanent genetic access to transiently active neurons via TRAP: targeted recombination in active populations. Neuron *78*, 773-784.

Kass, M., and Witkin, A. (1987). Analyzing oriented patterns. Computer vision, graphics, and image processing *37*, 362-385.

Kawashima, T., Kitamura, K., Suzuki, K., Nonaka, M., Kamijo, S., Takemoto-Kimura, S., Kano, M., Okuno, H., Ohki, K., and Bito, H. (2013). Functional labeling of neurons and their projections using the synthetic activity-dependent promoter E-SARE. Nat Methods *10*, 889-895.

Khan, A.R., Cornea, A., Leigland, L.A., Kohama, S.G., Jespersen, S.N., and Kroenke, C.D. (2015). 3D structure tensor analysis of light microscopy data for validating diffusion MRI. NeuroImage *111*, 192-203.

Klein, S., Staring, M., Murphy, K., Viergever, M.A., and Pluim, J.P. (2010). elastix: a toolbox for intensity-based medical image registration. IEEE Trans Med Imaging *29*, 196-205.

Mori, S., Crain, B.J., Chacko, V., and Van Zijl, P. (1999). Three-dimensional tracking of axonal projections in the brain by magnetic resonance imaging. Annals of neurology *45*, 265-269.

Sanz, E., Yang, L., Su, T., Morris, D.R., McKnight, G.S., and Amieux, P.S. (2009). Cell-type-specific isolation of ribosome-associated mRNA from complex tissues. Proc Natl Acad Sci U S A *106*, 13939-13944.

Tainaka, K., Kubota, S.I., Suyama, T.Q., Susaki, E.A., Perrin, D., Ukai-Tadenuma, M., Ukai, H., and Ueda, H.R. (2014). Whole-body imaging with single-cell resolution by tissue decolorization. Cell *159*, 911-924.

Tye, K.M., Prakash, R., Kim, S.Y., Fenno, L.E., Grosenick, L., Zarabi, H., Thompson, K.R., Gradinaru, V., Ramakrishnan, C., and Deisseroth, K. (2011). Amygdala circuitry mediating reversible and bidirectional control of anxiety. Nature *471*, 358-362.

Wang, H., Lenglet, C., and Akkin, T. (2015). Structure tensor analysis of serial optical coherence scanner images for mapping fiber orientations and tractography in the brain. Journal of biomedical optics *20*, 036003.

Ye, L., Kleiner, S., Wu, J., Sah, R., Gupta, R.K., Banks, A.S., Cohen, P., Khandekar, M.J., Bostrom, P., Mepani, R.J.*, et al.* (2012). TRPV4 is a regulator of adipose oxidative metabolism, inflammation, and energy homeostasis. Cell *151*, 96-110.